

Morphology changes in the evolution of liquid two-layer films

Andrey Pototsky, Michael Bestehorn, and Domnic Merkt

*Lehrstuhl für Theoretische Physik II,
Brandenburgische Technische Universität Cottbus,
Erich-Weinert-Straße 1, D-03046 Cottbus, Germany*

Uwe Thiele

*Max-Planck-Institut für Physik komplexer Systeme,
Nöthnitzer Straße 38, D-01187 Dresden, Germany*

Abstract

We consider a thin film consisting of two layers of immiscible liquids on a solid horizontal (heated) substrate. Both, the free liquid-liquid and the liquid-gas interface of such a bilayer liquid film may be unstable due to effective molecular interactions relevant for ultrathin layers below 100 nm thickness, or due to temperature-gradient caused Marangoni flows in the heated case. Using a long wave approximation we derive coupled evolution equations for the interface profiles for the general non-isothermal situation allowing for slip at the substrate. Linear and nonlinear analyses of the short- and long-time film evolution are performed for isothermal ultrathin layers taking into account destabilizing long-range and stabilizing short-range molecular interactions. It is shown that the initial instability can be of a varicose, zigzag or mixed type. However, in the nonlinear stage of the evolution the mode type and therefore the pattern morphology can change via switching between two different branches of stationary solutions or via coarsening along a single branch.

PACS numbers: 68.15.+e, 81.16.Rf, 68.55.-a, 47.20.Ky

I. INTRODUCTION.

Instabilities of thin liquid films between a solid substrate and a gas atmosphere have attracted much scientific interest. The main focus lies thereby on front instabilities of moving contact lines^{1,2,3} or on instabilities of the free liquid-gas interface of a flat film^{4,5,6}. A recent review can be found in Ref.7. To analyze such instabilities a long-wave or lubrication approximation^{7,8,9} is often used as a very powerful tool especially for low Reynolds number film flows. At present the basic behavior of one-layer films in the physically different thickness ranges is well understood. Several instability mechanisms exist that by means of different driving forces may destabilize an initially flat film. They are described, analysed and modelled in a large number of experimental^{4,5,10,11,12,13,14} and theoretical^{17,15,16,17,18,19,20,21,22,23,24,25,26,27,28,29,30,31} works. For film thicknesses d less than about 100 nm, effective molecular interactions between the film surface and the substrate dominate all the other forces, like thermo- and soluto-capillarity or gravity, and thus determine the film stability. For heated films of thicknesses above 100 nm, eventually thermocapillary forces become the most important influence leading to an instability caused by large-scale Marangoni convection^{5,29}. It is dominant up to an upper limit of the film thickness determined by the competition between large-scale and small-scale convection modes³². For even thicker films with thicknesses above 100 μm also the gravity force becomes important. Depending on its direction it may stabilize the large-scale Marangoni instability or destabilize the film further (Rayleigh-Taylor instability)^{18,19}. The lubrication approximation is valid up to a limiting film thickness obtained by the requirement that the wave length of the dominant instability mode λ_m is much larger than the film thickness d , i.e. $\lambda_m \gg d$. For the Rayleigh-Taylor instability λ_m depends on the interfacial tension, the density of the liquid and the gravitational acceleration but not on the film thickness⁷. It is of the order of 10^3 to $10^4 \mu\text{m}$ implying an upper limit for the film thickness of 10^2 to $10^3 \mu\text{m}$.

The stability and evolution of liquid films of thicknesses below 100 nm is determined by effective molecular interactions between substrate and film arising, for instance, from Van der Waals, electrostatic or entropic interactions^{33,34}. Such films are linearly unstable if the energy of the intermolecular interaction is a convex function of the film thickness. For film thicknesses above 10 nm the long-range Van der Waals forces dominate. They can be of different nature depending on the molecular properties of the involved media. One

distinguishes interactions between two randomly orienting dipoles (orientation interaction), between a randomly orienting dipole and an induced dipole (induction interaction), and between a fluctuating dipole and an induced dipole (dispersion interaction). Between two parallel interfaces at a distance d , all these forces decay as A/d^3 where A is the Hamaker constant³³. An unstable situation corresponds to a positive Hamaker constant. Note, however that different schools use different sign conventions. The dominant wave length of the instability λ_m increases monotonically with d as $\lambda \sim d^2$ (see Ref. 7). The stability of a film may change dramatically for a substrate coated with a layer of different dielectric properties as, for instance, a silicon substrate (Si) coated with an silicon oxide layer (SiO)³⁵. There, for an oxide layer of about 2 nm only ultrathin polystyrene (PS) films below 4 nm thickness are linearly unstable. Increasing the film thickness in the linearly unstable range, the wave length λ increases rapidly and diverges at the critical thickness d_c . For $d > d_c$ the film is linearly stable, but may rupture due to finite disturbances.

Imagine one replaces the (solid) coating layer by a liquid layer transforming the system in a two-layer liquid film. Some of the results obtained for a solid coating can be directly transferred to the new situation. The stability of the (now) upper layer still depends on the (now liquid) coating layer. However, additionally the liquid coating layer itself may be unstable making a re-evaluation of the stability necessary. This thought experiment leads quite naturally to the extension of the well studied one-layer systems to two-layer systems that are the subject of the present work. In general, there exist two possible two-layer geometries. On the one hand the two liquid layers can be situated between two solid plates leaving only the interface between the two liquids free to move. In consequence such a system can be described by a single evolution equation^{36,37,38}. On the other hand the two layers can be situated between a solid substrate and a gas atmosphere. Then both, the liquid-liquid and the liquid-gas interface are free to move and their evolution has to be described by coupled evolution equations. Models were derived, for instance, assuming a lower liquid layer that is much thicker than the upper layer³⁹, and for two-layer systems with surfactants (and non-newtonian behaviour)^{40,41,42} or including evaporation^{43,44,45}. A two-layer system under the solely influence of molecular interactions is studied in Ref. 46. In Ref. 47 a similar system is studied, however, the evolution equations are given in terms of variations of an energy functional.

The experimental interest in two-layer liquid films is up to now mainly focused on the

dewetting of a liquid layer from a very thick layer, i.e. a liquid bulk substrate^{48,49,50,51,52}. In contrast Ref. 53 studies the dewetting of a polystyrene (PS) layer of 15 to 68 nm thickness from a 46 nm thick polyamide (PA) layer. The substrate is a silicon (Si) wafer covered with a layer of native oxide. At high temperature (195°C) and small thicknesses (15...35 nm) the PS layer is unstable and dewets exhibiting typical spinodal patterns. At low temperature (115°C) the PA layer is solid resulting in a stable PS layer, independent of its thickness.

Ref. 54 studies relatively thick layers (100 nm to 1 μ m thickness) of poly(dimethylsiloxane) (PDMS) layers on a liquid substrate of fluorinated PDMS. They show that the PDMS films are metastable and may dewet by nucleation of holes. The velocity of the growth of holes depends on the viscosity and thickness of the substrate. In another system (PS layer on poly(methylmethacrylate) (PMMA) layer, both with thicknesses of about 100 nm) the dewetting velocity was found to exhibit a minimum as a function of the viscosity of the lower layer⁵¹. Furthermore, for a polycarbonate (PC) layer on a poly(styrene-*co*-acrylonitrile) (SAN) layer Ref. 52 reports a non-trivial dependence of the dewetting velocity on both layer thicknesses.

Recently we presented coupled evolution equations for two-layer liquid films taking into account long-range Van der Waals interactions only⁴⁷. This allows to study pathways towards rupture but can not describe the long-time evolution of such films as, for instance, necessary for the description of the above mentioned experiments. In the present paper we present the derivation of the system of evolution equations for a general interaction energy and a non-isothermal situation and then study the short- and long-time evolution of two-layer liquid films incorporating long-range and short-range interactions. Thereby the main focus lies on ultrathin layers with respective thicknesses below 100 nm for which the effective molecular interactions between the four media are the dominant influence.

The paper is structured as follows. The problem is formulated in Section II A followed by the derivation of the relevant long wave evolution equations for a general non-isothermal case allowing also for slip at the substrate. Focusing on the isothermal case without slip these equations are analyzed and integrated numerically in the subsequent sections. Section III presents the linear stability analysis for flat films starting from the general case in Section III A, focusing on long-range van der Waals interactions in Section III B, discussing the possible mode types in Section III C and introducing important limiting cases in Section III D. In Section IV we investigate the non-linear behaviour discussing in Section IV A

non-uniform stationary solutions as extrema of the Lyapunov functional, presenting in Section IV B two different pathways for mode-changes in the course of the time evolution, and discussing long-time stationary solutions for different experimentally relevant systems in Section IV C. Concluding remarks follow in Section V. Expressions for the surface tension gradients in terms of gradients of the layer thicknesses are discussed in an Appendix.

II. DERIVATION OF COUPLED LARGE-AMPLITUDE EVOLUTION EQUATIONS

A. General case

First, we derive coupled evolution equations for the profiles of the liquid-liquid interface $h_1(x, y)$ and the liquid-gas interface $h_2(x, y)$. We assume that the layers are thin enough that convective terms can be neglected. Considering a two-dimensional geometry as sketched in Fig. 1 the respective Stokes equations for the two layers are

$$\nabla(p_i + \phi_i) = \mu_i \Delta \vec{v}_i, \quad (1)$$

where $i = 1, 2$ denotes the respective layer. For each layer $\vec{v}_i = (u_i, w_i)$ is the velocity field, p_i the pressure, ϕ_i the potential of the bulk forces and μ_i the viscosity. The constant mean film thicknesses are denoted by $d_1 = (\int_0^L h_1 dx)/L$ and $d_2 = (\int_0^L h_2 dx)/L$ where L is the lateral system size. A lubrication approximation⁷ is applied assuming the ratio of vertical and horizontal length scales to be small. As smallness parameter we use the ratio $\epsilon = d_1/\lambda$ where λ is the characteristic lateral length scale of the film instability. In zeroth order in ϵ the Stokes equations (1) simplify to

$$\mu_2 \partial_z^2 u_2 = \partial_x \bar{p}_2 \quad (2)$$

$$\partial_z \bar{p}_2 = 0 \quad (3)$$

$$\mu_1 \partial_z^2 u_1 = \partial_x \bar{p}_1 \quad (4)$$

$$\partial_z \bar{p}_1 = 0, \quad (5)$$

where the \bar{p}_i stand for $p_i + \phi_i$. At the substrate ($z = 0$) we use a Navier slip and a no-penetration condition, i.e.

$$u_1 = \beta \partial_z u_1 \quad \text{and} \quad w_1 = 0, \quad (6)$$

respectively. The slip length is denoted by β . At the liquid-liquid interface ($z = h_1$) we use the continuity of the velocity field, the kinematic condition and the continuity of the tangential component of the liquid stress tensor

$$u_1 = u_2, \quad w_1 = w_2, \quad (7)$$

$$w_1 = \partial_t h_1 + u_1 \partial_x h_1, \quad (8)$$

$$(9)$$

and

$$\mu_1 \partial_z u_1 - \mu_2 \partial_z u_2 = \partial_x \sigma_{12}, \quad (10)$$

respectively. The normal stress condition is discussed below. At the liquid-gas interface ($z = h_2$) only the kinematic condition and the continuity of the tangential component of the liquid stress tensor apply, i.e.

$$w_2 = \partial_t h_2 + u_2 \partial_x h_2, \quad (11)$$

$$\mu_2 \partial_z u_2 = \partial_x \sigma_2. \quad (12)$$

The σ_{12} and σ_2 stand for the interfacial tensions of the liquid-liquid and of the liquid-gas interface, respectively. The boundary conditions for the normal component of the stress tensor are written incorporating the disjoining pressures at the liquid-liquid $\Pi_1(h_1, h_2)$ and at the liquid-gas $\Pi_2(h_1, h_2)$ interface, respectively. They represent effective molecular interactions between the interfaces that result, for instance, from Van der Waals interactions³³. They are discussed in detail below. For the liquid-gas interface ($z = h_2$) we obtain

$$p_2(h_2) - p_0 = -\sigma_2 \partial_x^2 h_2 + \Pi_2(h_1, h_2)$$

and for the liquid-liquid interface ($z = h_1$)

$$p_1(h_1) - p_2(h_1) = -\sigma_{12} \partial_x^2 h_1 + \Pi_1(h_1, h_2), \quad (13)$$

where p_0 is the constant pressure in the gas atmosphere. Eqs. (13) can be written in terms of variations of an energy functional $F[h_1, h_2]$

$$\begin{aligned} p_1(h_1) - p_2(h_1) &= \frac{\delta F}{\delta h_1} \\ p_2(h_2) - p_0 &= \frac{\delta F}{\delta h_2}, \end{aligned} \quad (14)$$

with

$$F = \int \left(\sigma_1 \frac{(\partial_x h_1)^2}{2} + \sigma_2 \frac{(\partial_x h_2)^2}{2} + f(h_1, h_2) \right) dx, \quad (15)$$

and $f(h_1, h_2)$ being the free energy of the flat films per unit area.

Equations (2) and (4) are integrated three times with respect to z to obtain the stream functions Ψ_i , defined by ($w_i = -\partial_x \Psi_i$, $u_i = \partial_z \Psi_i$). The six x -dependent integration constants are determined using the boundary conditions (6), (7), (10), and (12). Thus the velocity fields in the two layers are given by

$$\begin{aligned} u_1 &= \frac{1}{\mu_1} (\partial_x \bar{p}_1) \frac{z^2}{2} + \frac{1}{\mu_1} (z + \beta) K_1 \\ u_2 &= \frac{1}{\mu_2} (\partial_x \bar{p}_2) \frac{z^2}{2} + \frac{1}{\mu_2} K_2 (z - h_1) - \frac{\partial_x \bar{p}_2}{\mu_2} \frac{h_1^2}{2} + u_1(h_1), \end{aligned} \quad (16)$$

with $K_1 = K_2 + \partial_x \sigma_{12} + [(\partial_x \bar{p}_2) - (\partial_x \bar{p}_1)] h_1$ and $K_2 = \partial_x \sigma_2 - (\partial_x \bar{p}_2) h_2$.

The stream functions Ψ_i are related to the flow in the lower layer $\Gamma_1 = \int_0^{h_1} u_1 dz$ and to the one in the upper layer $\Gamma_2 = \int_{h_1}^{h_2} u_2 dz$ by $\Gamma_1 = \Psi_1(h_1)$, $\Gamma_1 + \Gamma_2 = \Psi_2(h_2)$. Using the Ψ_i we rewrite Eqs. (8) and (11) to obtain the evolution equations for the two interface profiles

$$\partial_t h_1 + \partial_x [\Psi_1(h_1)] = 0, \quad (17)$$

$$\partial_t h_2 + \partial_x [\Psi_2(h_2)] = 0. \quad (18)$$

Written in terms of the energy functional they read

$$\begin{aligned} \partial_t h_1 &= \partial_x \left[Q_{11} \partial_x \frac{\delta F}{\delta h_1} + Q_{12} \partial_x \frac{\delta F}{\delta h_2} - D_{11} \partial_x \sigma_{12} - D_{12} \partial_x \sigma_2 \right] \\ \partial_t h_2 &= \partial_x \left[Q_{21} \partial_x \frac{\delta F}{\delta h_1} + Q_{22} \partial_x \frac{\delta F}{\delta h_2} - D_{21} \partial_x \sigma_{12} - D_{22} \partial_x \sigma_2 \right], \end{aligned} \quad (19)$$

with the mobility matrices of the pressure terms

$$\mathbf{Q} = \frac{1}{\mu_1} \begin{pmatrix} \frac{h_1^3}{3} + \beta h_1^2 & \frac{h_1^2}{2} (h_2 - \frac{h_1}{3}) + \beta h_1 h_2 \\ \frac{h_1^2}{2} (h_2 - \frac{h_1}{3}) + \beta h_1 h_2 & \frac{(h_2 - h_1)^3}{3} (\frac{\mu_1}{\mu_2} - 1) + \frac{h_2^3}{3} + \beta h_2^2 \end{pmatrix} \quad (20)$$

and of the tangential stress terms

$$\mathbf{D} = \frac{1}{\mu_1} \begin{pmatrix} \frac{h_1^2}{2} + \beta h_1 & \frac{h_1^2}{2} + \beta h_1 \\ h_1 (h_2 - \frac{h_1}{2}) + \beta h_2 & \frac{\mu_1 (h_2 - h_1)^2}{2\mu_2} + h_1 (h_2 - \frac{h_1}{2}) + \beta h_2 \end{pmatrix}, \quad (21)$$

respectively. Note, that the mobility matrix \mathbf{Q} is symmetric and all mobilities Q_{ik} and D_{ik} are positive. Dropping the terms representing the effective molecular interactions, Eqs. (19)

represent the fully nonlinear equivalent for the weakly nonlinear equations derived in Ref. 55, 56. Assuming that the interfacial tensions are influenced by thermocapillarity only, one can express the derivatives $\partial_x \sigma_{12}$ and $\partial_x \sigma_2$ in terms of gradients of local thicknesses $\partial_x h_i$. This is done in the Appendix.

For isothermal ultrathin liquid films one has ($\partial_x \sigma_{12} = \partial_x \sigma_2 = 0$). The situation is then relaxational (or variational), i.e. Eqs. (19) possess a Lyapunov functional, namely the energy functional F , which decreases monotonously in time as shown next. The total time derivative of the Lyapunov functional is $dF/dt = \int \left(\frac{\delta F}{\delta h_1} \partial_t h_1 + \frac{\delta F}{\delta h_2} \partial_t h_2 \right) dx$. Expressing $\partial_t h_i$ by Eqs. (19) and using partial integration with periodic boundary conditions, one obtains

$$\frac{dF}{dt} = - \int \sum_{i,k} Q_{ik} \left(\partial_x \frac{\delta F}{\delta h_i} \right) \left(\partial_x \frac{\delta F}{\delta h_k} \right) dx. \quad (22)$$

Because

$$\det \mathbf{Q} = \frac{(h_2 - h_1)^3 h_1^3}{9\mu_1 \mu_2} + \frac{1}{12\mu_1^2} h_1^4 (h_2 - h_1)^2 + \beta \left(\frac{h_1^3}{3\mu_1^2} (h_2 - h_1)^2 + h_1^2 \frac{(h_2 - h_1)^3}{3\mu_1 \mu_2} \right) > 0 \quad (23)$$

and $Q_{ii} > 0$, the quadratic form in Eq. (22) is positive definite implying $dF/dt < 0$. The existence of F allows to identify the stationary solutions of Eqs. 19 with the extrema of F . This will be used below in Section IV A.

B. The disjoining pressures $\Pi_i(h_1, h_2)$

In many important cases, as for instance, for polymer films on apolar substrates^{4,14}, the interaction energy is mainly determined by its long-range apolar dispersion part. However, if the model only takes into account a destabilizing long-range interaction the time evolution definitively leads to rupture of the upper or lower layer⁴⁷ making it impossible to study the long-time coarsening behaviour. To be able to study the long-time evolution one has to include stabilizing short-range interactions^{20,33} into the model. Although these are normally not included for films of thicknesses above 10 nm because they do not change the stability of flat films, also for such films they become important in the non-linear stage of evolution when the local thicknesses become comparable to their interaction length.

The long-range part of the interaction energy for each pair of interfaces (see Fig.1) resulting from dispersive Van der Waals interactions is given by $A_{ijkl}/2\pi h^2$ (see Ref.33), where A_{ijkl} is a (four-index) Hamaker constant which corresponds to the interaction between

the interfaces $i-j$ and $k-l$. Each index in A_{ijkl} can be one out of $g, 1, 2$ and s , denoting gas, liquid 1, liquid 2 and substrate, respectively. The four-index Hamaker constant is calculated using an equivalent of Eq. (11.13) of Ref. 33 that is based on the assumption that the main absorption frequencies of all involved media are about $\nu_e = 3 \times 10^{15}$ Hz and that the zero frequency contribution is negligible. One uses

$$A_{ijkl} \approx \frac{3h\nu_e}{8\sqrt{2}} \frac{(n_i^2 - n_j^2)(n_l^2 - n_k^2)}{(n_i^2 + n_j^2)^{1/2}(n_l^2 + n_k^2)^{1/2}[(n_i^2 + n_j^2)^{1/2} + (n_l^2 + n_k^2)^{1/2}]}, \quad (24)$$

where n_i are the refractive indices of the media. The three-index Hamaker constants are given by

$$A_{ijk} = A_{ijjk}. \quad (25)$$

The short-range forces which can be of an electrostatic or structural nature^{17,57} decay exponentially with h . The electrostatic part results from the formation of diffuse electric double-layers in the vicinity of interfaces involving polar liquids^{58,59,60,61}. For films with thicknesses in the range of the Debye length the diffuse double-layers at the two interfaces overlap resulting in a repulsive or attractive force between the interfaces. The corresponding interaction energy between the interfaces $s-1$ and $1-2$ is given by $S_1 \exp[(l_0 - h_1)/l_1]$ and between the interfaces $1-2$ and $2-g$ by $S_2 \exp[(l_0 - (h_2 - h_1))/l_2]$, where $l_0 = 0.158$ nm is the Born repulsion length, and $l_1, l_2 \sim 1..10$ nm are the interaction lengths of the short-range interactions²⁰. Further on we consider the two correlation lengths l_1 and l_2 to be equal and denote them by l . $S_1 > 0$ and $S_2 > 0$ are the short-range components of the total spreading coefficients. They are related to the lower layer on the substrate below a bulk of the upper liquid and to the upper layer on the lower film as substrate below the ambient gas, respectively. We do not take into account short-range interactions between interfaces $s-1$ and $2-g$.

Collecting the long-range and the short-range forces the disjoining pressures $\Pi_1(h_1, h_2)$ and $\Pi_2(h_1, h_2)$ are specified as

$$\begin{aligned} \Pi_1(h_1, h_2) &= \frac{A_{21s}}{6\pi h_1^3} - \frac{A_{12g}}{6\pi(h_2 - h_1)^3} - \frac{S_1}{l_1} \exp\left[\frac{l_0 - h_1}{l_1}\right] + \frac{S_2}{l_2} \exp\left[\frac{l_0 - (h_2 - h_1)}{l_2}\right] \\ \Pi_2(h_1, h_2) &= \frac{A_{12g}}{6\pi(h_2 - h_1)^3} + \frac{A_{g21s}}{6\pi h_2^3} - \frac{S_2}{l_2} \exp\left[\frac{l_0 - (h_2 - h_1)}{l_2}\right] \end{aligned} \quad (26)$$

To non-dimensionalize Eqs. (19) we scale the thicknesses with l , the lateral coordinate x with $\lambda = l(d_2 - d_1)\sqrt{2\pi\sigma_1/|A_{12g}|}$, and time t with $\tau = (2\pi)^2\sigma_1\mu_1 l(d_2 - d_1)^4/A_{12g}^2$. Then the

scaled energy functional

$$F = \int \left[\frac{1}{2}(\partial_x h_1)^2 + \frac{\sigma}{2}(\partial_x h_2)^2 - \frac{\bar{A}_{12g}}{6(h_2 - h_1)^2} - \frac{\bar{A}_{21s}}{6h_1^2} - \frac{\bar{A}_{g21s}}{6h_2^2} + c_1(h_1 - \bar{d}_1) + c_2(h_2 - \bar{d}_2) + \bar{S}_1 \exp(-h_1) + \bar{S}_2 \exp(h_1 - h_2) \right] dx, \quad (27)$$

involves the scaled Hamaker constants $\bar{A}_{ijkl} = [(d_2 - d_1)/l]^2 A_{ijkl}/|A_{12g}|$, spreading coefficients $\bar{S}_i = 2\pi [(d_2 - d_1)]^2 S_i \exp(d_0/l)/|A_{12g}|$, and mean layer thicknesses $\bar{d}_i = d_i/l$. The c_i are Lagrange multipliers that ensure mass conservation for the two liquids. The corresponding energy scale is $|A_{12g}|/2\pi(d_2 - d_1)^2$ and the ratios of the mean layer thicknesses, surface tensions and viscosities are $d = d_2/d_1$, $\sigma = \sigma_2/\sigma_1$ and $\mu = \mu_2/\mu_1$, respectively. Further on, we denote the scaled variables using the same symbols as before, i.e. the scaled mean thicknesses are given by d_i and the local thicknesses by h_i . The non-dimensional mobility matrices are obtained from Eqs. (20) and (21) by dropping the factor $1/\mu_1$ and replacing β by β/l .

III. LINEAR STABILITY

A. General stability of flat films

We start the analysis of our model for two-layer films by discussing the linear stability of flat films with $h_1(x) = d_1$ and $h_2(x) = d_2$. Eqs. (19) are linearized in $\epsilon \ll 1$ for small amplitude disturbances $\epsilon \chi_i \exp(\gamma t) \exp(kx)$ for $i = 1, 2$ where k , γ and $\chi = (\chi, 1)$ are the wave number, growth rate and amplitudes of the disturbance, respectively. The dispersion relation $\gamma(k)$ is obtained by solving the resulting eigenvalue problem $(\mathbf{J} - \gamma \mathbf{I})\chi = 0$.

For the isothermal case ($\partial_x \sigma_{12} = \partial_x \sigma_2 = 0$ in Eqs. (19)), the corresponding *non*-symmetric Jacobi matrix \mathbf{J} is given by $\mathbf{J} = -k^2 \mathbf{Q} \cdot \mathbf{E}$, where \mathbf{Q} is the scaled mobility matrix. \mathbf{E} is the energy matrix

$$\mathbf{E} = \begin{pmatrix} \frac{\partial^2 f}{\partial h_1^2} + k^2 & \frac{\partial^2 f}{\partial h_1 \partial h_2} \\ \frac{\partial^2 f}{\partial h_1 \partial h_2} & \frac{\partial^2 f}{\partial h_2^2} + \sigma k^2 \end{pmatrix}, \quad (28)$$

where $f(h_1, h_2)$ is the local part of the energy density from Eq. (27). This yields

$$\gamma = \frac{\text{Tr}}{2} \pm \sqrt{\frac{\text{Tr}^2}{4} - \text{Det}}, \quad (29)$$

where $\text{Tr} = -k^2[2Q_{12}E_{12} + Q_{11}E_{11} + Q_{22}E_{22}]$ and $\text{Det} = k^4 \det \mathbf{Q} \det \mathbf{E}$ are the trace and the determinant of \mathbf{J} . Since $\det \mathbf{Q} \neq 0$ the eigenvalue problem can be written as the generalized

eigenvalue problem $(k^2 \mathbf{E} + \gamma \mathbf{Q}^{-1}) \boldsymbol{\chi} = 0$. Because \mathbf{E} and \mathbf{Q}^{-1} are both symmetric and \mathbf{Q}^{-1} is positive definite one can deduce that all eigenvalues γ are real⁶² as expected for a variational problem. In the non-isothermal case, the Jacobi matrix is given by $\mathbf{J} = -k^2(\mathbf{Q} \cdot \mathbf{E} - \mathbf{D} \cdot \boldsymbol{\Gamma})$, where $\boldsymbol{\Gamma}$ is a scaled matrix of coefficients for the Marangoni terms. It is defined in Section A. Neither the matrix \mathbf{D} nor $\boldsymbol{\Gamma}$ are symmetric. This leads to (in general) complex eigenvalues indicating the possibility of oscillating motion in the non-isothermal case^{55,56}.

Going back to the isothermal case, inspection of the generalized eigenvalue problem shows that the stability threshold is completely determined by the eigenvalues of \mathbf{E} . Since the surface tension terms are always positive, the onset of the instability is always found for $k = 0$, i.e. the system is linearly stable, independently of the wavelength of the disturbance, for

$$\det \mathbf{E} > 0 \quad \text{and} \quad E_{11} > 0 \quad \text{at} \quad k = 0. \quad (30)$$

An instability sets in if at least one of the conditions (30) is violated. Then the flat two-layer film is unstable to disturbances with k larger zero and smaller than a cutoff wavenumber

$$k_c^2 = -\frac{1}{2} \left(\frac{\partial^2 f}{\partial h_1^2} + \frac{1}{\sigma} \frac{\partial^2 f}{\partial h_2^2} \right) \pm \sqrt{\frac{1}{4} \left(\frac{\partial^2 f}{\partial h_1^2} - \frac{1}{\sigma} \frac{\partial^2 f}{\partial h_2^2} \right)^2 + \frac{1}{\sigma} \left(\frac{\partial^2 f}{\partial h_1 \partial h_2} \right)^2} \quad (31)$$

determined by the condition $\det \mathbf{E}(k_c) = 0$.

Fig. 2 shows a schematic stability diagram in the plane (E_{11}, E_{22}) . The stability threshold $E_{11} E_{22} = E_{12}^2$, $E_{11} > 0$ is a hyperbola, represented by the solid line. The unstable region below and left of that line is divided by a second hyperbola into a two-mode and a one-mode region. In the two-mode region both growth rates given by Eq. (29) are positive for k smaller than the respective cut-off k_c . In the one-mode region only one γ is positive for $k < k_c$. Fixing all other system parameters, $\det \mathbf{E}(k)$ is determined by k . If at $k = 0$ the system is in the two-mode region, then by increasing k one passes two times a line $\det \mathbf{E} = 0$, as indicated by the dashed arrow in Fig. 2. At each crossing a growth rates (Eq. (29)) becomes negative, i.e. a mode is stabilized. If at $k = 0$ the system is in the one-mode region the line $\det \mathbf{E} = 0$ is crossed only once (dot-dashed line).

B. Long-range interaction only

As detailed above the stabilizing short-range interaction only becomes important if at least one layer thickness is locally comparable to the interaction length l , i.e. if a layer

becomes thinner than about 10 nm. Therefore, to study the linear stability of thicker layers one can neglect the short-range terms in Eq. (27). In this case, Eq. (30) is used to study the role of the Hamaker constants Eq. (24) in the linear evolution of the system. First we note that the Hamaker constants are coupled through the refractive indices of the media n_i . This allows only for selected combinations of signs of the A_{ijk} and A_{ijkl} as given in Table I.

For fixed Hamaker constants, i.e. fixed combination of materials, $\det \mathbf{E}_0 = \det \mathbf{E}(k=0)$ is a function of the ratio d of the layer thicknesses only. Using Table I one can show that for positive $\partial^2 f / \partial h_i^2$ the equation $\det \mathbf{E}_0(d) = 0$ can only have the solution $d = 1$, i.e. $d_2 - d_1 = 0$. This means that only for vanishing upper layer the system can be on the stability threshold. In consequence the stability threshold can *not* be crossed by solely changing the ratio of layer thicknesses. This was analyzed in Ref. 47 for a variety of experimentally studied systems. Increasing the ratio d from one the system remains either completely in the unstable or in the stable region.

To compare the stability behaviour of two-layer and one-layer films we introduce two effective one-layer films as follows. In (1) we assume the lower layer to be solid, i.e. we regard the upper layer as a one-layer film on a coated substrate. In (2) we assume the upper layer to be rigid but deformable by bending. The lower liquid layer corresponds then to a one-layer film on a solid bulk substrate. In case (1) the one-layer liquid film is unstable if the second derivative of the energy with respect to the film thickness h_2 is negative, $\partial^2 f / h_2^2 < 0$. The stability threshold at $\partial^2 f / h_2^2 = 0$ can be crossed by changing the layer thickness $h_2 - h_1$ or the thickness of the coating layer h_1 . This was demonstrated in Refs. 63 and 14 for a PS film on Si wafers covered with a 1.6 nm thick SiO layer. In case (2) the one-layer liquid film is unstable for $\partial^2 f / h_1^2 < 0$. It can also be destabilized by changing the layer thicknesses, as was shown in Ref. 64 for a rigid PS layer on top of a liquid PDMS layer on a Si substrate.

Comparing the stability thresholds for the two effective one-layer systems to the stability diagram in Fig. 2 shows that the stability threshold of the two-layer system lies in the region where both effective one-layer systems are stable. This indicates that a two-layer system is always less stable than corresponding effective one-layer systems.

C. Different instability modes

The stability threshold can be studied in rather general terms as was done above because its main features do not depend on surface tensions or viscosities. However, this is not the case for the characteristics of the instability like mode type, growth rates or dominant wave length. To discuss these we focus in the following on selected two-layer films studied experimentally^{51,63,65}. We consider various combinations of layers of polystyrene (PS), poly(methylmethacrylate) (PMMA) and poly(dimethylsiloxane) (PDMS) on a silicon (Si) or on a silicon-oxide (SiO) substrate. The Hamaker constants for different combinations are calculated using Eq. (24) and given in Table II.

The linear instability of a two-layer film has two different modes. It can be of zigzag or varicose type. For the former the deflections of the two interfaces are in phase whereas for the latter they are in anti-phase. For special parameter values one can also find a mixed type, where modes are present because they have equal fastest growth rates⁴⁷.

The model studied in Ref. 39 assumes a thick lower layer thereby neglecting the interaction between the substrate and the liquid-liquid and the liquid-gas interface. In this case only the varicose mode can be unstable. In the general case, however, also the zigzag mode can become unstable. Both modes are normally asymmetric, i.e. the deflection amplitudes of the two interfaces differ. We characterize this asymmetry by $\phi = \chi/(1 + \chi^2)$. Negative (positive) ϕ corresponds to varicose (zigzag) modes. The value $|\phi| = 1/2$ represents the symmetric case, whereas $\phi = 0$ corresponds to maximal asymmetry, i.e. one of the interfaces is flat. The asymmetry increases with the ratio of the surface tensions σ . Note, that the dispersion relation and the type of the dominant mode depend on σ and μ , whereas the stability diagram Fig. 2 *does not*.

The two mode types are plotted in Fig. 3 for a Si/PMMA/PS/air system for a fixed value of d and different ratios of viscosities μ . The dispersion relations $\gamma(k)$ are shown together with the corresponding ϕ . We show here that the type of the dominant mode can be changed by varying d or μ . It can also change in dependence of the ratio of the interfacial tensions σ as studied in Ref. 47.

Strictly speaking, the concept of the mode type characterized by ϕ is only valid in the linear stage of the evolution. However, to discuss morphology changes we generalize this concept to nonlinear thickness profiles $h_i(x)$. We define a generalized mode or solution type

by the integral

$$\phi_{\text{int}} = \frac{1}{L} \int \frac{(h_1 - d_1)(h_2 - d_2)}{[(h_1 - d_1)^2 + (h_2 - d_2)^2]} dx, \quad (32)$$

taken over the domain length L . In many cases the sign of the product $(h_1 - d_1)(h_2 - d_2)$ does not depend on x allowing to 'read' the mode type directly from the plots of the layer profiles. For small deflection amplitudes Eq. (32) gives again the linear mode type defined above. In the following we use the notion 'mode-type' in the linear and in the nonlinear regime.

D. Limiting cases

For general d_i the radical in Eq. (29) does not allow to give an analytic expression for the wave number k_m and the characteristic growth time $\tau_m = 1/\gamma_m$ of the fastest growing mode. Nevertheless, one can derive asymptotic expressions for k_m and τ_m in the two important limiting cases of (1) small thickness of the upper layer $d_2 - d_1 \ll d_2$ and (2) small thickness of the lower layer $d_1 \ll d_2$. First consider case (1), which corresponds to a liquid film (the upper layer) on a liquid substrate (the very thick lower layer). The dimensional k_m and τ_m are then given by

$$\begin{aligned} k_m &= \frac{1}{(d_2 - d_1)^2} \sqrt{\frac{|A_{12g}|}{4\pi\sigma_{\text{eff}}}} \\ \tau_m &= \frac{16(2\pi)^2\sigma_{\text{eff}}\mu_1(d_2 - d_1)^6}{d_1 A_{12g}^2}, \end{aligned} \quad (33)$$

with $\sigma_{\text{eff}} = \sigma_1\sigma_2/(\sigma_1 + \sigma_2)$. Note that all variables are in their dimensional form.

Interestingly, the growth time τ_m depends only on the viscosity of the lower layer μ_1 and does not depend on μ_2 . This can be explained by the fact that the flow in the lower layer which is related to μ_1 , is much larger than that in the upper one³⁹. At constant thickness of the lower layer, τ_m is proportional to $(d_2 - d_1)^6$, i.e. a liquid film on a bulk liquid substrate evolves faster than the same film on a solid substrate (growth time $\sim (d_2 - d_1)^5$) and even faster than the same film on a solid substrate with slippage (growth time $\sim (d_2 - d_1)^5 / [1 + 3\beta/(d_2 - d_1)]$).

In case (2), which corresponds to a liquid film (the lower layer) on a solid substrate below

the other liquid (the very thick upper layer), the dimensional k_m and τ_m are given by

$$\begin{aligned} k_m &= \frac{1}{d_1^2} \sqrt{\frac{A_{21s}}{4\pi\sigma_1}} \\ \tau_m &= \frac{12(2\pi)^2\sigma_1\mu_1 d_1^5}{A_{21s}^2}. \end{aligned} \quad (34)$$

Note that in case (2) k_m and τ_m coincide with k_{low} and τ_{low} , respectively, the characteristics of the dominant mode of the instability of a liquid film below a bulk liquid calculated using one-layer theory. A discussion of this geometry for a Rayleigh-Taylor instability can be found in Refs. 18 and 66.

E. Long-range apolar and short-range polar interactions

The stability analysis based only on long-range interactions becomes incorrect for layer thicknesses in the range of the interaction length l of short-range interactions. Practically, the latter become important (well) below 10 nm layer thickness. In contrast to the result for the exclusive action of long-range van der Waals forces, in the regime where both, short- and long-range interactions, are important the stability threshold can be crossed by changing the layer thicknesses d_i . Fig. 4 presents a selection of qualitatively different stability diagrams in the plane spanned by the layer thicknesses obtained when varying the strength of the short-range interaction for a fixed long-range interaction.

By changing the short-range part of the spreading coefficient S_1 and S_2 one finds seven topologically different types of such diagrams. These types correspond to regions in the (S_1, S_2) plane as indicated in Fig. 5. In the absolute unstable region bounded on the right by $(S_1)_{\min} = (e/4)^4 A_{21s}/|A_{12g}|$ and above by $(S_2)_{\min} = (e/4)^4$ the system can not be stabilized by changing d_1 or d_2 . Only if at least one of the two S_i is larger than the corresponding critical value (a) stable region(s) can be found in the $(d_1, d_2 - d_1)$ plane (see Fig. 4). For $S_1 > (S_1)_{\min}$ a stable region exists that extends towards infinite $(d_2 - d_1)$, as shown in Figs. 4(a), (b) and (d). Thereby, for large $(d_2 - d_1)$ the system is stable for $(d_1)_{\min} < d_1 < (d_1)_{\max}$, where $(d_1)_{\max}$ and $(d_1)_{\min}$ are the solutions of the equation $A_{21s}/|A_{12g}| = S_1 x^4 \exp(-x)$. Similarly, for $S_2 > (S_2)_{\min}$ a stable region exists that extends towards infinite d_1 , as in Figs. 4(a) to (d). For large d_1 the system is stable for $(d_2 - d_1)_{\min} < d_2 < (d_2 - d_1)_{\max}$, where $(d_2 - d_1)_{\max}$ and $(d_2 - d_1)_{\min}$ are the solutions of the equation $1 = S_2 x^4 \exp(-x)$. In the gray shaded triangle at the center of Fig. 5 an additional bounded stable region exists in the $(d_1, d_2 - d_1)$

plane (see Figs. 4(b) and (c)). Combining the different conditions gives the following seven types of stability diagrams.

- I:** The stable region is continuous and extends in respective stripes towards infinite d_1 and $d_2 - d_1$ (Fig. 4(a)).
- II:** There exist two separated stable regions, one extending towards infinite d_1 and the other one towards infinite $d_2 - d_1$ (Fig. 4(d)).
- III:** Similar to Type II but with an additional bounded stable region (Fig. 4(b)).
- IV:** A bounded stable region exists together with an unbounded region extending towards infinite d_1 (Fig. 4(c)).
- V:** Similar to type IV but with the unbounded region extending towards infinite $(d_2 - d_1)$ (not shown).
- VI:** Only one stable region exists extending towards infinite d_1 (not shown).
- VII:** Similar to type VI but with the unbounded region extending towards infinite $(d_2 - d_1)$ (not shown).

Further on we will focus our attention on the stability diagram of type I.

IV. NON-LINEAR BEHAVIOUR

A. Stationary solutions as extrema of the Lyapunov functional

To find periodic stationary solutions of the scaled Eqs. (19), the time derivatives $\partial_t h_i$ are set to zero. Integration yields

$$\begin{aligned} Q_{11} \partial_x \left(\frac{\delta F}{\delta h_1} \right) + Q_{12} \partial_x \left(\frac{\delta F}{\delta h_2} \right) &= C_1 \\ Q_{21} \partial_x \left(\frac{\delta F}{\delta h_1} \right) + Q_{22} \partial_x \left(\frac{\delta F}{\delta h_2} \right) &= C_2, \end{aligned} \quad (35)$$

where the C_i are constants and F is given by Eq. (27). Note that the left hand sides of Eqs. (35) represent the flow in the lower layer and the total flow, respectively. For a stationary state both flows are zero, i.e. the $C_1 = C_2 = 0$. Because the mobility matrix \mathbf{Q}

is non-singular, one concludes from Eqs. (35) that the stationary states of the Eqs. (19) are the extrema of the Lyapunov functional F , i.e. they are solutions of

$$\begin{aligned} -\partial_{xx}h_1 + \frac{\partial f}{\partial h_1} &= c_1 \\ -\sigma\partial_{xx}h_2 + \frac{\partial f}{\partial h_2} &= c_2, \end{aligned} \tag{36}$$

where f denotes the local part of Eq. (27) and the constants c_i correspond to the Lagrangian multipliers introduced in Section II A. To obtain a finite amplitude solution for given mean thicknesses we use continuation techniques^{67,68,69}. We start with analytically known stationary periodic small-amplitude profiles, which correspond to the linear eigenfunctions for the critical wave number k_c . By continuation we follow the family of solutions changing the period L . We characterize the solutions by the deflection amplitudes A_1 and A_2 , the energy E , the norm $L_2 = (1/L) \int [(h_1 - d_1)^2 + (h_2 - d_2)^2] dx$ and the integral mode type ϕ_{int} . To determine the stability of the stationary solutions $h_i(x)$, we add small perturbations $\delta h_i(x) \sim \exp(\beta t)$ to both interfaces $h_i(x)$, linearize the full time-dependent evolution equations (19) around $h_i(x)$ and solve the obtained eigenvalue problem $\mathbf{L}(h_i, \partial_x h_i, \partial_x) \delta \mathbf{h}(x) = \beta \delta \mathbf{h}(x)$ for the linear operator \mathbf{L} after discretizing it in space. The sign of the largest eigenvalue β determines the stability of the stationary solution. Note that due to the translational invariance of the evolution equations (19), there exists always a symmetry mode $\delta h_i(x) = \partial_x h_i(x)$ with the eigenvalue $\beta = 0$.

B. Mode type transitions

The type of the dominant instability mode calculated above by linear stability may not persist in the course of the nonlinear evolution. Possible mode type changes may have a dramatic effect on the (observable) overall morphology of the film. We investigate these changes by studying both, the evolution in time of the film profiles and the stationary solutions obtained by continuation.

The evolution in time is obtained by numerical simulations of the scaled coupled evolution equations Eqs. (19) in a one-dimensional periodic domain. Both, semi-implicit pseudo-spectral and explicit time integration schemes are used. Initial conditions consist of flat layers with an imposed noise of amplitude 0.001.

1. Transition via branch switching

First the time evolution of an initially flat film is studied for parameters as in Fig. 3 (a) using a domain size equal to four times the fastest growing wave length λ_m . A time sequence of snap shots is shown in Fig. 6. In the early stage of the evolution a varicose mode develops ($t = 8.1$) as expected from the linear analysis. Then in a sub-domain of size λ_m the deflection amplitudes increase dramatically accompanied by a morphological change towards a zigzag type profile ($t = 9.7$). This is further illustrated by the dependence of the integral mode-type (Eq. 32) on time given in Fig. 7(b). Further on, the length of the zigzag part increases slightly, and coarsening sets in resulting in the disappearance of one varicose-type drop ($t = 16.4$). Next one of the remaining drops increases its amplitude and flips to a zigzag type hole ($t = 20.6$). Finally the last remaining varicose-type drop disappears ($t \approx 28$), and the system approaches a stationary (but not stable) state. The evolution of the relative energy of the profile in time is given in Fig. 7(a). It is seen very clearly that the phases of very slow evolution correspond to solutions that are close to stationary solutions. This results from the fact that the (unstable) stationary solutions form saddle points in function space that are approached along their stable manifolds and subsequently repel the system along their unstable manifolds (for a discussion see Ref. 70) The evolution stops after a further coarsening step, when the period becomes equal to the system size (not shown).

To explain the observed mode-type change, we study the stationary solutions of the evolution equations Eqs. (19). We find a family of solutions starting at the subcritical primary bifurcation, then turning three times at saddle-node bifurcations (folds) and going towards infinite periods (see Fig. 8(a)). A stability analysis using the solution period as the period of the disturbance (thereby excluding coarsening modes) shows that two branches are stable (solid lines) and two are unstable (dashed lines). Along the first unstable branch, which starts at L_c and ends at the first fold at $L \approx 60$ the energy E is always larger than the one of the flat film E_0 (Fig. 8(b)), and it increases with decreasing period. This subcritical branch corresponds to nucleation solutions that have to be overcome to break the film in parts smaller than L_c (see Ref. 26 for a discussion of this type of solutions for a one-layer system). The first stable branch starts at the first fold at $L \approx 59$ and ends at the second fold at $L \approx 116$. Its relative energy decreases monotonically with increasing period. Mostly it is energetically preferable to the flat film. The second unstable branch (between the

second fold at $L \approx 116$ and the third fold at $L \approx 79$) turns back towards smaller periods. The second stable branch starts at the third fold and goes towards infinite periods. Its energy decreases rapidly from values even above the flat film to values below the ones of the first stable branch. The energy of the second unstable branch is always larger than the energies of both stable branches. This indicates that it corresponds to nucleation solutions, or critical solutions that have to be overcome to switch between the two stable branches. Along the second unstable branch, the mode-type changes from varicose to zigzag (Fig. 8 (d)) explaining the non-trivial behavior observed in the time evolution shown in Fig. 6. There are two stable solutions with a period equal to the dominant linear wave length ($\lambda_m \approx 108$) (see Fig. 9). The one of higher energy that is approached first in the time evolution is of varicose type whereas the one of lower energy that the system switches to is of zigzag type (cp. Fig. 8(b)). A transition between the two solutions is accompanied by a strong increase of the amplitude A_1 (see Fig. 8(a)).

2. *Transition via coarsening*

A mode-type change is not always connected to a transition between different branches of stationary solutions. Also coarsening along one branch may lead to such a change if the mode-type varies along the branch. To demonstrate this, we simulate the time evolution using parameters as in Fig. 3(b). A time sequence of profiles and the corresponding evolution of the relative energy and the integral mode-type are shown in Figs. 10 and 11, respectively. Early in the evolution the layer profiles represent a zigzag mode ($t = 6.0$) corresponding to the linear results (Fig. 3(b)). Then, within the very short period of time from $t = 6.0$ to 10.8, nonlinear effects result in a first change towards a varicose type profile, as shown in the inset of Fig. 11(b). Then the system approaches the branch of stationary solutions. As a result the evolution slows down and the pattern begins to coarsen. With ongoing coarsening ($t > 10.8$) the size of the droplets increases ($t = 135$, $t = 461$) and at very late times ($t > 490$) the mode type changes back to zigzag type (Fig. 11(b)). Here, the amplitudes of the interfaces do not change dramatically, as was the case in Section IV B 1. In this sense the transition is continuous. The characteristics of the corresponding stationary solutions are shown in Fig. 12. The primary bifurcation is again subcritical (Fig. 12(a)) the solution family continues towards smaller periods until turning at a saddle-node bifurcation (fold)

and heading towards infinite periods. The subcritical branch is unstable with energies higher than the energy of the flat film (Fig. 12(b)). The second branch starting at the fold ($L \approx 26$) consists of solutions whose energy decreases monotonically with increasing period. They are stable to disturbances of identical period but unstable to coarsening modes. Fig. 12 (d) shows that the solution with the period equal to $\lambda_m = 50.81$ is of varicose type. The corresponding layer profile is shown in Fig. 13(a) together with the profile after the first coarsening step. When the period becomes larger than 94.2, the solution changes to zigzag type (Fig. 12(d)) as shown in Fig. 13(b). This explains the mode-type change found in the time evolution (Fig. 10).

Here we have restricted our attention to a parameter set corresponding to region I of Fig. 5, i.e. corresponding to the stability diagram shown in Fig. 4 (a). The existence of a stable branch of stationary solutions which continues towards infinite period implies that the rupture of the two layers is completely avoided by the short-range repulsion. However, this may not be the case for parameter ranges belonging to the other types of stability diagrams. A detailed analysis of the stationary solutions for all types will be done elsewhere.

C. Large-period stationary solutions

The stability of the numerical code, used to solve the evolution equations Eqs. (19), requires a very small time step $t = 0.00001$. As a result it takes very long even to reach the final stationary solution in a system of size $4\lambda_m$ using 256 grid points. It is not feasible at the moment to study many coarsening steps in this way. However, one can rely on continuation techniques that use an adaptive spatial grid along the continuation path⁶⁹ to obtain stationary solutions of arbitrarily large periods that correspond to solutions that would be obtained in a time evolution at very late times. We show in Fig. 14 possible large-period stationary solutions for different physical systems that are investigated experimentally. One finds qualitatively different morphologies like a drop of the lower liquid 'looking through' a nearly flat film of the upper layer for a Si/PMMA/PS/air system. Note however that also the upper layer is continuous (due to the stabilizing short-range interaction), i.e. also the drop is covered by a very thin layer of the upper liquid. This is more pronounced for a SiO/PS/PDMS/air system. In contrast, for a SiO/PMMA/PS/air system one finds a drop of the upper liquid 'swimming' on the lower liquid that however is attracted towards the

base of the drop. These equilibrium solutions are equivalents of drop configurations studied in Ref. 71 for macroscopic (but smaller than the capillary length) drops. However, here the mesoscopic contact angles are not given explicitly but result from the underlying effective molecular interactions, i.e. the short- and long-range forces used.

V. CONCLUSION

We have derived coupled non-linear evolution equations for the profiles of the liquid-liquid and liquid-gas interfaces of a thin two-layer liquid film heated from below allowing for slip at the substrate. We have shown that in the isothermal case the evolution equations can be written in terms of variations of an appropriate Lyapunov functional F which monotonically decreases in time. The stability conditions for flat layers have been given in terms of F . We have shown that a two-layer film is less stable than related effective one-layer films introduced in Section III B. Even if both effective one-layer films are stable the two-layer film may be unstable if the determinant of the energy matrix $\det \mathbf{E}$ is negative.

We have shown that if the Hamaker constants are given by the usual expression (Eq. (24)), i.e. they are coupled through the refractive indices, and no other forces are present, the stability of the flat films with thicknesses of (~ 100 nm) can not be changed by solely changing the layer thicknesses. Incorporating a stabilizing short-range interaction the stability can be changed in this way. We have classified the resulting possible types of stability diagrams in the space of the layer thicknesses and given a 'phase diagram' in terms of the short-range parts of the spreading coefficients for the occurrence of the different types of stability diagrams.

In general, the linear stability analysis of the flat film has shown that both, varicose or zigzag mode, may be unstable depending on the ratios of the layer thicknesses, viscosities and surface tensions (see also Ref. 47). This seems to be in contrast to Ref. 39. However, the difference arises because there it is assumed that the lower layer is thick compared to the upper layer neglecting thereby all interactions with the substrate. Then the zigzag mode is always stable.

The introduction of the stabilizing short-range interaction allows to study the long-time evolution and stationary layer profiles. Possible stationary states have then been determined as extrema of the Lyapunov functional F . The resulting bifurcation diagrams show a rich

branch structure that depends strongly on parameter values. We have focused on one type of stability diagram where a stable branch going towards infinite period always exists. This implies the existence of a non-ruptured stationary state in the long-time limit also in the time evolution.

We have found that the mode type of a profile may change during the evolution of an instability on three ways. First, the profile type changes in the course of the short-time evolution. This is connected to different mode types found for the dominant linear mode and the stationary solution of equal period on the solution branch approached first in the time evolution. It seems that this behaviour is more probable for a subcritical primary bifurcation. In the case studied here this change is from zigzag to varicose. In the nonlinear regime the profile can change its type by (i) jumping from one to another stable branch and by (ii) coarsening along a single stable branch. Combinations of the different ways may also be possible. We have found that for the parameters considered here both nonlinear transitions go from varicose towards zigzag type. In case (i) the transition occurs without change of the period, but with a dramatic increase in amplitude of the profile. In the case (ii) the transition occurs continuously without amplitude jump because mediated by coarsening a small-period varicose mode turns into a large-period zigzag one.

In all examples considered here (except the SiO/PMMA/PS/air system with $d_1 = 30$, $d_2 = 50$) we have found a zigzag-type solution at large periods. For the future it would be very interesting to further analyze the stationary solutions for a broader range of experimentally interesting systems like the ones studied in Refs. 52,63. This should clarify under which conditions the long-time (or large-period) solutions are energetically preferable and determine how 'late' the transition may occur. A systematic analysis of all types of stability diagrams would also discuss metastability and absolute stability of the flat two-layer films. Furthermore, we are very optimistic that the evolution equations presented here will serve to study the questions of hole growth and possible front instabilities in the dewetting of a liquid layer on a liquid substrate of finite thickness^{50,52}.

APPENDIX A

To further specify the thermocapillar part of Eqs. 19 we rewrite the derivatives $\partial_x \sigma_{12}$ and $\partial_x \sigma_2$ in terms of the gradients of the local thicknesses $\partial_x h_i$. In the long-wave approximation⁷

the temperature field is in both layers a linear function of the vertical coordinate z , i.e. $T_i = a_i z + b_i$. To determine the coefficients we consider a three-layer geometry (Fig. 15), i.e. we take into account the heat conduction in a gas layer of finite thickness $d_g = d_t - d_2$, where d_t is the distance between the substrate and an upper plate. The temperature in the gas layer is $T_g = a_g z + b_g$. The boundary conditions at both interfaces are continuity of the temperature field and continuity of the heat flux $\kappa_i \partial_z T_i = \kappa_k \partial_z T_k$, where κ_i is the thermal conductivity of the i -th layer. The temperatures at the substrate T_0 and at the upper plate T_t are constant. The coefficients a_i and b_i depend on the local thicknesses h_i and are given by

$$a_g = \frac{\alpha \Delta T}{d_t - h_2 + \frac{\kappa_g}{\kappa_1} h_1 + \frac{\kappa_g}{\kappa_2} (h_2 - h_1)}$$

$$a_2 = \frac{a_g \kappa_g}{\kappa_2}, \quad a_1 = \frac{a_g \kappa_g}{\kappa_1}$$

$$b_1 = T_0, \quad b_g = T_t - a_g d_t$$

$$b_2 = a_g \kappa_g h_1 \left(\frac{1}{\kappa_1} - \frac{1}{\kappa_2} \right) + T_0,$$

where $\Delta T = T_0 - T_2$ and

$$\alpha = \frac{d_2 - d_t - \kappa_g h_1 / \kappa_1 - \kappa_g (d_2 - d_1) / \kappa_2}{\kappa_g h_1 / \kappa_1 - \kappa_g (d_2 - d_1) / \kappa_2}.$$

Here T_2 is the temperature of the liquid-gas interface, when both interfaces are undeformed, i.e. for $h_i = d_i$. The above formulas allow to determine the derivatives

$$\partial_x \sigma_{12} = \Gamma_{11} \partial_x h_1 + \Gamma_{12} \partial_x h_2 \quad (\text{A1})$$

$$\partial_x \sigma_2 = \Gamma_{21} \partial_x h_1 + \Gamma_{22} \partial_x h_2,$$

where the matrix $\mathbf{\Gamma}$ is determined as follows

$$\mathbf{\Gamma} = a \begin{pmatrix} \frac{\kappa_g}{\kappa_1} \frac{d\sigma_1}{dT} b & -\frac{\kappa_g}{\kappa_1} \frac{d\sigma_1}{dT} h_1 \left(\frac{\kappa_g}{\kappa_2} - 1 \right) \\ \frac{d\sigma_2}{dT} (bc - \frac{\kappa_g}{\kappa_2} h_2 b) & \frac{d\sigma_2}{dT} \left\{ \frac{\kappa_g}{\kappa_2} (d_t + h_1 b) - b h_1 \left(\frac{\kappa_g}{\kappa_2} - 1 \right) \right\} \end{pmatrix}. \quad (\text{A2})$$

Here $a = (\alpha \Delta T) / \left[d_t - h_2 + \frac{\kappa_g}{\kappa_1} h_1 + \frac{\kappa_g}{\kappa_2} (h_2 - h_1) \right]^2$, $b = \kappa_g (1/\kappa_1 - 1/\kappa_2)$ and $c = \left\{ d_t - h_2 \left(1 - \frac{\kappa_g}{\kappa_2} \right) \right\}$. For the linear normal Marangoni effect $d\sigma_{12}/dT$ and $d\sigma_2/dT$ are negative and constant. The Eqs. (A2) are used in Eqs. (19) to obtain a closed system of equations for h_1 and h_2 .

-
- ¹ A. M. Cazabat, F. Heslot, S. M. Troian, and P. Carles, *Nature* **346**, 824 (1990).
- ² F. Brochard-Wyart and P. de Gennes, *J. Phys.: Cond. Mat* **6**, A9 (1993).
- ³ A. L. Bertozzi, A. Münch, X. Fanton, and A. M. Cazabat, *Phys. Rev. Lett.* **81**, 5169 (1998).
- ⁴ G. Reiter, *Phys. Rev. Lett.* **68**, 75 (1992).
- ⁵ S. J. VanHook, M. F. Schatz, W. D. McCormick, J. B. Swift, and H. L. Swinney, *Phys. Rev. Lett.* **75**, 4397 (1995).
- ⁶ U. Thiele, M. Mertig, and W. Pompe, *Phys. Rev. Lett.* **80**, 2869 (1998).
- ⁷ A. Oron, S. H. Davis, and S. G. Bankoff, *Rev. Mod. Phys.* **69**, 931 (1997).
- ⁸ O. Reynolds, *Phil. Trans. Roy. Soc.* **177**, 157 (1886).
- ⁹ A. Sommerfeld, *Z. Math. Phys.* **50**, 97 (1904).
- ¹⁰ A. Sharma and G. Reiter, *J. Colloid Interface Sci.* **178**, 383 (1996).
- ¹¹ G. Reiter, *Langmuir* **9**, 1344 (1993).
- ¹² K. Jacobs, R. Seemann, G. Schatz, and S. Herminghaus, *Langmuir* **14**, 4961 (1998).
- ¹³ S. J. VanHook, M. F. Schatz, J. B. Swift, W. D. McCormick, and H. L. Swinney, *J. Fluid Mech.* **345**, 45 (1997).
- ¹⁴ R. Seemann, S. Herminghaus, and K. Jacobs, *Phys. Rev. Lett.* **86**, 5534 (2001).
- ¹⁵ E. Ruckenstein and R. K. Jain, *J. Chem. Soc. Faraday Trans. II* **70**, 132 (1974).
- ¹⁶ M. B. Williams and S. H. Davis, *J. Colloid Interface Sci.* **90**, 220 (1982).
- ¹⁷ P. G. de Gennes, *Rev. Mod. Phys.* **57**, 827 (1985).
- ¹⁸ S. G. Yiantsios and B. G. Higgins, *Phys. Fluids A* **1**, 1484 (1989).
- ¹⁹ A. Oron and P. Rosenau, *J. Physique II France* **2**, 131 (1992).
- ²⁰ A. Sharma, *Langmuir* **9**, 861 (1993).
- ²¹ A. Sharma, *Langmuir* **9**, 3580 (1993).
- ²² V. S. Mitlin, *J. Colloid Interface Sci.* **156**, 491 (1993).
- ²³ A. Sharma and R. Khanna, *Phys. Rev. Lett.* **81**, 3463 (1998).
- ²⁴ U. Thiele, M. G. Velarde, and K. Neuffer, *Phys. Rev. Lett.* **87**, 016104 (2001).
- ²⁵ E. Schäffer and U. Steiner, *Eur. Phys. J. E* **8**, 347 (2002).
- ²⁶ U. Thiele, K. Neuffer, Y. Pomeau, and M. G. Velarde, *Colloid Surf. A* **206**, 135 (2002).
- ²⁷ U. Thiele, *Eur. Phys. J. E* **12**, 409 (2003).

- ²⁸ A. L. Bertozzi, G. Grün, and T. P. Witelski, *Nonlinearity* **14**, 1569 (2001).
- ²⁹ M. Bestehorn, A. Pototsky, and U. Thiele, *Eur. Phys. J. B* **33**, 457 (2003).
- ³⁰ U. Thiele and E. Knobloch, *Physica D* **190**, 213 (2004).
- ³¹ A. Pototsky, M. Bestehorn, and U. Thiele, *Physica D* **199**, 138 (2004).
- ³² A. A. Golovin, A. A. Nepomnyashchy, and L. M. Pismen, *Phys. Fluids* **6**, 34 (1994).
- ³³ J. N. Israelachvili, *Intermolecular and Surface Forces* (Academic Press, London, 1992).
- ³⁴ R. J. Hunter, *Foundation of Colloid Science*, vol. 1 (Clarendon Press, Oxford, 1992).
- ³⁵ R. Seemann, S. Herminghaus, and K. Jacobs, *J. Phys.-Cond. Mat.* **13**, 4925 (2001).
- ³⁶ Z. Q. Lin, T. Kerle, S. M. Baker, D. A. Hoagland, E. Schäffer, U. Steiner, and T. P. Russell, *J. Chem. Phys.* **114**, 2377 (2001).
- ³⁷ Z. Q. Lin, T. Kerle, T. P. Russell, E. Schäffer, and U. Steiner, *Macromolecules* **35**, 3971 (2002).
- ³⁸ D. Merkt, A. Pototsky, M. Bestehorn, and U. Thiele, *Phys. Fluids* (2005), (submitted).
- ³⁹ F. Brochard-Wyart, P. Martin, and C. Redon, *Langmuir* **9**, 3682 (1993).
- ⁴⁰ Y. L. Zhang, O. K. Matar, and R. V. Craster, *J. Colloid Interface Sci.* **262**, 130 (2003).
- ⁴¹ R. V. Craster and O. K. Matar, *J. Fluid Mech.* **425**, 235 (2000).
- ⁴² O. K. Matar, R. V. Craster, and M. R. E. Warner, *J. Fluid Mech.* **466**, 85 (2002).
- ⁴³ K. D. Danov, V. N. Paunov, N. Alleborn, H. Raszillier, and F. Durst, *Chem. Eng. Sci.* **53**, 2809 (1998).
- ⁴⁴ K. D. Danov, V. N. Paunov, S. D. Stoyanov, N. Alleborn, H. Raszillier, and F. Durst, *Chem. Eng. Sci.* **53**, 2823 (1998).
- ⁴⁵ V. N. Paunov, K. D. Danov, N. Alleborn, H. Raszillier, and F. Durst, *Chem. Eng. Sci.* **53**, 2839 (1998).
- ⁴⁶ D. Bandyopadhyay, *Stability and dynamics of bilayers* (2001), master-thesis, Dep. Chem. Eng., Ind. Inst. Tech. Kanpur.
- ⁴⁷ A. Pototsky, M. Bestehorn, D. Merkt, and U. Thiele, *Phys. Rev. E* **70**, 025201(R) (2004).
- ⁴⁸ O. Wunnicke, P. Müller-Buschbaum, M. Wolkenhauer, C. Lorenz-Haas, R. Cubitt, V. Leiner, and M. Stamm, *Langmuir* **19**, 8511 (2003).
- ⁴⁹ M. D. Morariu, E. Schäffer, and U. Steiner, *Phys. Rev. Lett.* **92**, 156102 (2004).
- ⁵⁰ A. Faldi, R. J. Composto, and K. I. Winey, *Langmuir* **11**, 4855 (1995).
- ⁵¹ P. Lambooy, K. C. Phelan, O. Haugg, and G. Krausch, *Phys. Rev. Lett.* **76**, 1110 (1996).
- ⁵² Q. Pan, K. I. Winey, H. H. Hu, and R. J. Composto, *Langmuir* **13**, 1758 (1997).

- ⁵³ C. Renger, P. Müller-Buschbaum, M. Stamm, and G. Hinrichsen, *Macromolecules* **33**, 8388 (2000).
- ⁵⁴ P. Martin, A. Buguin, and F. Brochard-Wyart, *Europhys. Lett.* **28**, 421 (1994).
- ⁵⁵ A. A. Nepomnyashchii and I. B. Simanovskii, *Pmm-J. Appl. Math. Mech.* **54**, 490 (1990).
- ⁵⁶ A. A. Nepomnyashchii and I. B. Simanovskii, *Q. J. Mech. Appl. Math.* **50**, 149 (1997).
- ⁵⁷ G. F. Teletzke, H. T. Davis, and L. E. Scriven, *Rev. Phys. Appl.* **23**, 989 (1988).
- ⁵⁸ B. V. Deryagin and L. D. Landau, *Acta Physicochim.* **14**, 633 (1941).
- ⁵⁹ E. J. W. Verwey and J. T. G. Overbeck, *Theory of the Stability of Lyophilic Colloids* (Elsevier, Amsterdam, 1948).
- ⁶⁰ H. Ohshima, *Colloid Polym. Sci.* **252**, 158 (1974).
- ⁶¹ H. Ohshima, *Colloid Polym. Sci.* **252**, 257 (1974).
- ⁶² E. S. Manteuffel and K. Vettors, *Lineare Algebra* (Teubner Verlagsgesellschaft, Leipzig, 1972).
- ⁶³ M. D. Morariu, E. Schäffer, and U. Steiner, *Eur. Phys. J. E* **12**, 375 (2003).
- ⁶⁴ M. O. David, G. Reiter, T. Sitthai, and J. Schultz, *Langmuir* **14**, 5667 (1998).
- ⁶⁵ M. Sferrazza, C. Xiao, R. A. L. Jones, D. G. Bucknall, J. Webster, and J. Penfold, *Phys. Rev. Lett.* **78**, 3693 (1997).
- ⁶⁶ S. G. Yiantsios and B. G. Higgins, *J. Colloid Interface Sci.* **147**, 341 (1991).
- ⁶⁷ E. Doedel, H. B. Keller, and J. P. Kernevez, *Int. J. Bif. Chaos* **1**, 493 (1991).
- ⁶⁸ E. Doedel, H. B. Keller, and J. P. Kernevez, *Int. J. Bif. Chaos* **1**, 745 (1991).
- ⁶⁹ E. Doedel, A. Champneys, T. Fairfrieve, Y. Kusnetzov, B. Sandstede, and X. Wang, *Continuation and Bifurcation Software for Ordinary Differential Equations* (Concordia University, Montreal, 1997).
- ⁷⁰ U. Thiele, L. Brusch, M. Bestehorn, and M. Bär, *Eur. Phys. J. E* **11**, 255 (2003).
- ⁷¹ L. Mahadevan, M. Adda-Bedia, and Y. Pomeau, *J. Fluid Mech.* **451**, 411 (2002).

TABLE I: Possible combinations of signs of the different Hamaker constants for given order of the refractive indices of the involved medias.

refractive indices	A_{12g}	A_{21s}	A_{g21s}
$n_s > n_1, n_1 < n_2, n_2 > n_g$	+	+	-
$n_s < n_1, n_1 < n_2, n_2 > n_g$	+	-	+
$n_s < n_1, n_1 > n_2, n_2 > n_g$	-	+	+
$n_s > n_1, n_1 > n_2, n_2 > n_g$	-	-	-

TABLE II: Hamaker constants for various combinations of polymers.

System	$A_{12g} \times 10^{-20}\text{Nm}$	$A_{21s} \times 10^{-20}\text{Nm}$	$A_{g21s} \times 10^{-20}\text{Nm}$
Si/PMMA/PS/air	1.49	3.8	-23.02
SiO/PMMA/PS/air	1.49	-0.024	0.15
SiO/PS/PDMS/air	-1.83	0.42	1.25

FIG. 1: Sketch of the problem in two dimensions. The local thickness of the lower layer is h_1 , the total local film thickness is h_2 .

FIG. 2: The schematic stability diagram for fixed coupling E_{12} . Shown are the stability threshold (solid line) and the boundary between the one-mode and the two-mode region (dotted line). Both are given by $\det \mathbf{E} = 0$ for increasing wave number k . Dashed and dot-dashed arrows represent parametric lines given by $(E_{11}(k)$ and $E_{22}(k))$. The dashed (dot-dashed) line starts at $k = 0$ in the two-mode (one-mode) region. At an intersection of a line $\det \mathbf{E}(k = 0)$ and a parametric line one of the growth rates changes its sign.

FIG. 3: Shown are the growth rate γ (solid lines) and the mode type ϕ (dashed lines) of the leading eigenmode. (a) A varicose mode from the one-mode region at $d_1 = 30$, $d_2 = 47$ and $\sigma = \mu = 1$, (b) a zigzag mode from the one-mode region at $d_1 = 15$, $d_2 = 40$ and $\sigma = \mu = 1$. Panel (c) gives γ and ϕ for d_1 and d_2 as in (b) but for $\mu = 0.1$. For convenience we plot in (b) 10γ and in (a) 20γ .

FIG. 4: Different types of stability diagrams in the plane of the layer thicknesses $(d_1, d_2 - d_1)$, shown for different strength of the short-range interactions S_1 and S_2 as given in the legends. The shaded parts represent linearly stable regions. The Hamaker constants are $A_{12g} = 1.49$, $A_{21s} = 3.8$, $A_{g21s} = -23.02$, corresponding to the Si/PMMA/PS/air system. Panels (a), (b), (c) and (d) correspond to ranges I, III, IV and II in Fig. 5, respectively.

FIG. 5: Phase diagram in the plane (S_1, S_2) for the Si/PMMA/PS/air system. The absolute stable region (hatched rectangle in the lower left corner) is bounded by $(S_1)_{\min} = (e/4)^4 A_{21s} / |A_{12g}|$ from the right and by $(S_2)_{\min} = (e/4)^4$ from above. The unstable region is divided into seven qualitatively different subregions, described in the main text.

FIG. 6: Snapshots of the time evolution of a Si/PMMA/PS/air system for $d_1 = 30, d_2 = 47$, $S_1 = S_2 = 1, \sigma = 1$ and $\mu = 1$ at times as given in the legends. The domain length is $L = 4\lambda_m$ and time is in units of $1/\gamma_m$.

FIG. 7: Evolution in time of (a) the relative energy $E - E_0$ and (b) the integral mode-type ϕ_{int} (Eq. 32) for parameters as in Fig. 6. Time is in units of $1/\gamma_m$. In (a) the dashed lines denote the energy levels which correspond to the stationary solutions with periods $L = \lambda_m$ (first and second line from above), $L = 4/3\lambda_m$ (third line from above) and $L = 2\lambda_m$ (the lowest line), taken from Fig. 8(b).

FIG. 8: Characterization of the stationary periodic solutions for the system of Fig. 7. Shown are (a) the amplitude of the lower layer A_1 , (b) the relative energy $E - E_0$, (c) the norm L_2 , and (d) the integral mode type ϕ_{int} in their dependence on the period L . In (d) the inset shows a zoom of the region marked by the dashed box.

FIG. 9: The two stationary solutions with period $L = 108.28$ (cp. Fig. 8) corresponding to the wave length of the relevant dominant linear mode λ_{max} . Shown are (a) the varicose type and (b) the zigzag type solution from the first and second stable branch, respectively.

FIG. 10: Snapshots of the time evolution of a Si/PMMA/PS/air system for $d_1 = 15$, $d_2 = 40$, $S_1 = S_2 = 1$, $\sigma = 1$ and $\mu = 1$ at times as given in the legends. The domain length is $L = 4\lambda_m$ and time is in units of $1/\gamma_m$.

FIG. 11: Evolution in time of (a) the relative energy $E - E_0$ and (b) the integral mode-type ϕ_{int} (Eq. 32) for parameters as in Fig. 10. The inset in (b) shows the early-time behaviour of the mode-type. Time is in units of $1/\gamma_m$. In (a) the dashed lines denote the energy levels which correspond to the stationary solutions with periods $L = \lambda_m$, $L = 4/3\lambda_m$ and $L = 2\lambda_m$, taken from Fig. 12(b).

FIG. 12: Characterization of the stationary periodic solutions, for the system of Fig. 10. Shown are (a) the amplitude of the upper layer A_2 , (b) the relative energy $E - E_0$, (c) the norm L_2 and (d) the integral mode type ϕ_{int} in their dependence on the period L .

FIG. 13: The two stationary solutions with period $L = 50.8$ and $L = 101.6$ (cp. Fig. 12) corresponding to once and twice the wave length of the dominant linear mode λ_{max} , respectively. To symbolize the coarsening process we show in (a) and (b) two and one period(s), respectively. The x coordinate is in units of λ_{max} .

FIG. 14: Large-period (long-time) stationary profiles for (a) a Si/PMMA/PS/air system with $d_1 = 30$, $d_2 = 39$, $\lambda_m = 132$ and period $L = 26 \times \lambda_m$, (b) a SiO/PMMA/PS/air with $d_1 = 30$, $d_2 = 50$, $\lambda_m = 246$ and period $L = 20 \times \lambda_m$, (c) a Si/PMMA/PS/air system with $d_1 = 30$, $d_2 = 70$, $\lambda_m = 118$ and $L = 21 \times \lambda_m$ and (d) a SiO/PS/PDMS/air with $d_1 = 30$, $d_2 = 70$, $\lambda_m = 557$ and $L = 10 \times \lambda_m$. The remaining parameters are $\sigma = 1$, $\mu = 1$, and $S_1 = S_2 = 1$.

FIG. 15: Sketch of the system with a gas layer of finite thickness.

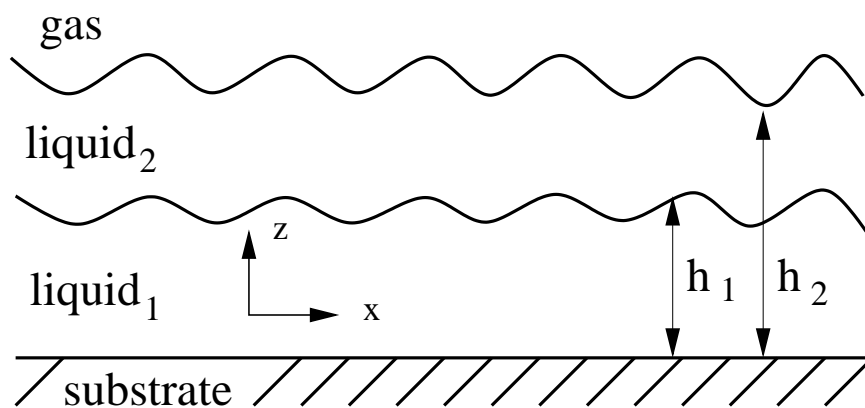


Fig. 1
Pototsky et al., J. Chem. Phys.

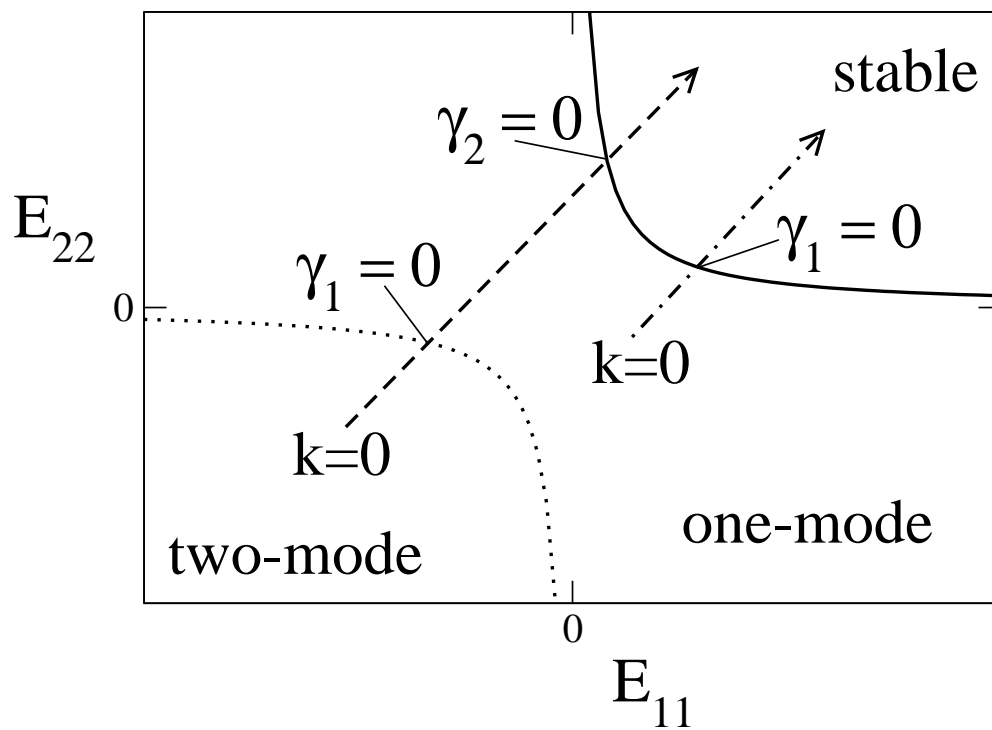


Fig. 2
 Pototsky et al., J. Chem. Phys.

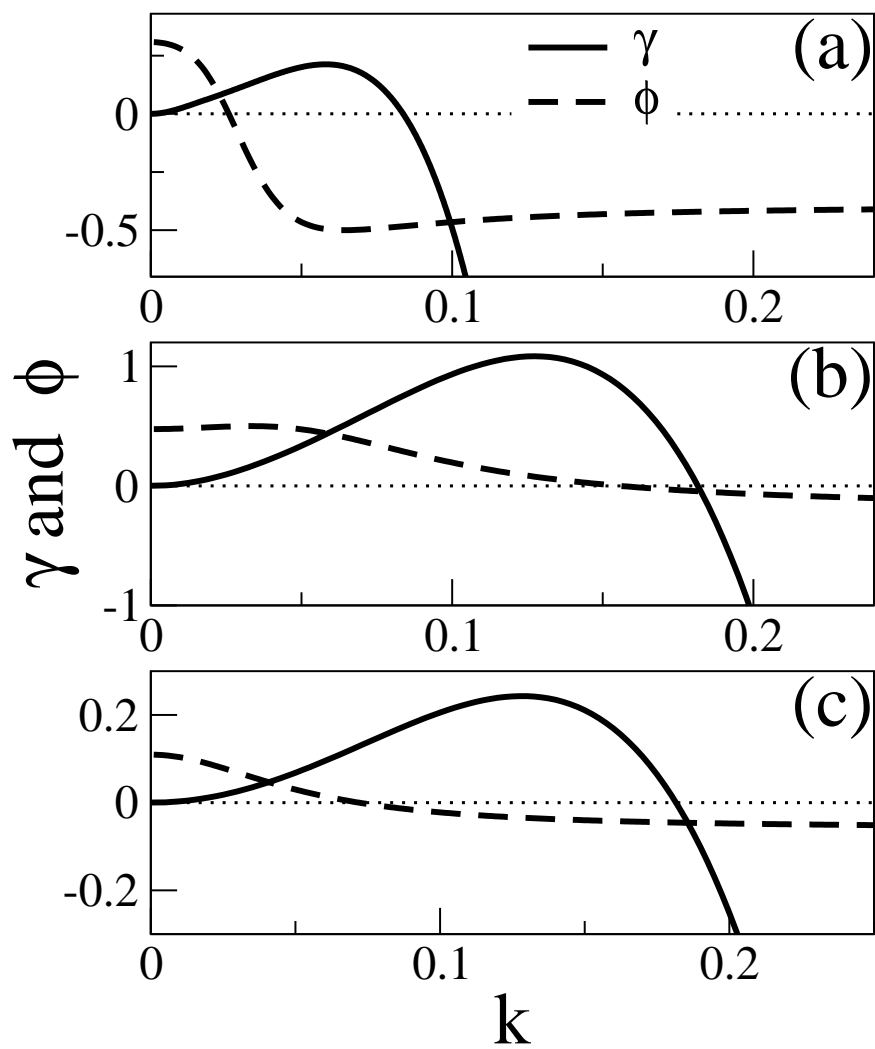


Fig. 3
Pototsky et al., J. Chem. Phys.

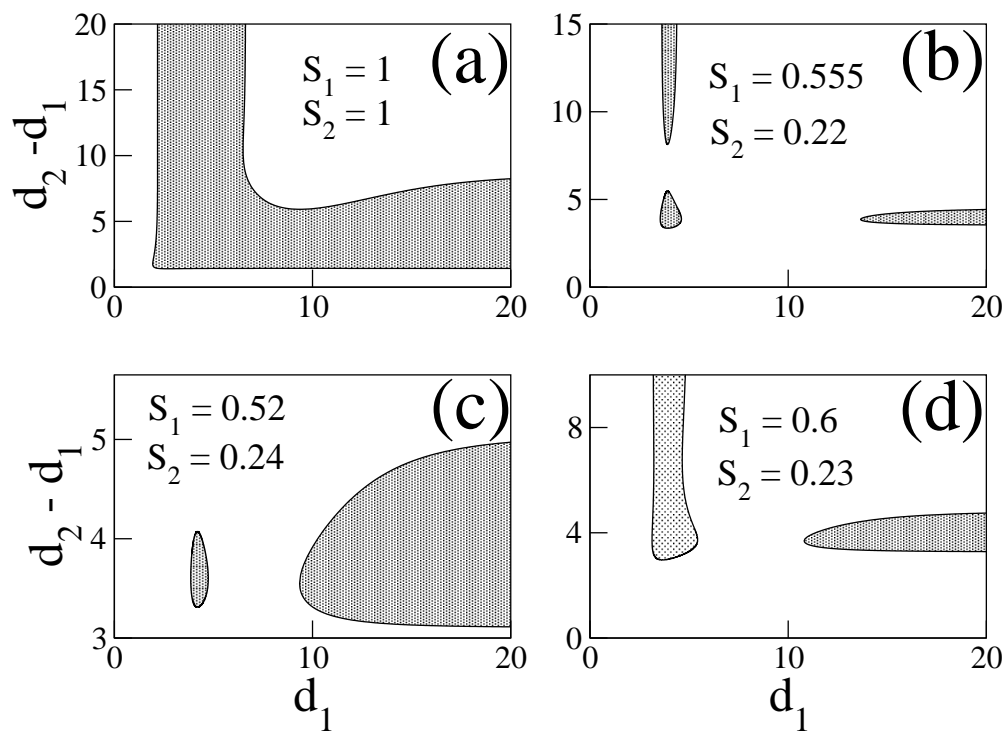


Fig. 4
 Pototsky et al., J. Chem. Phys.

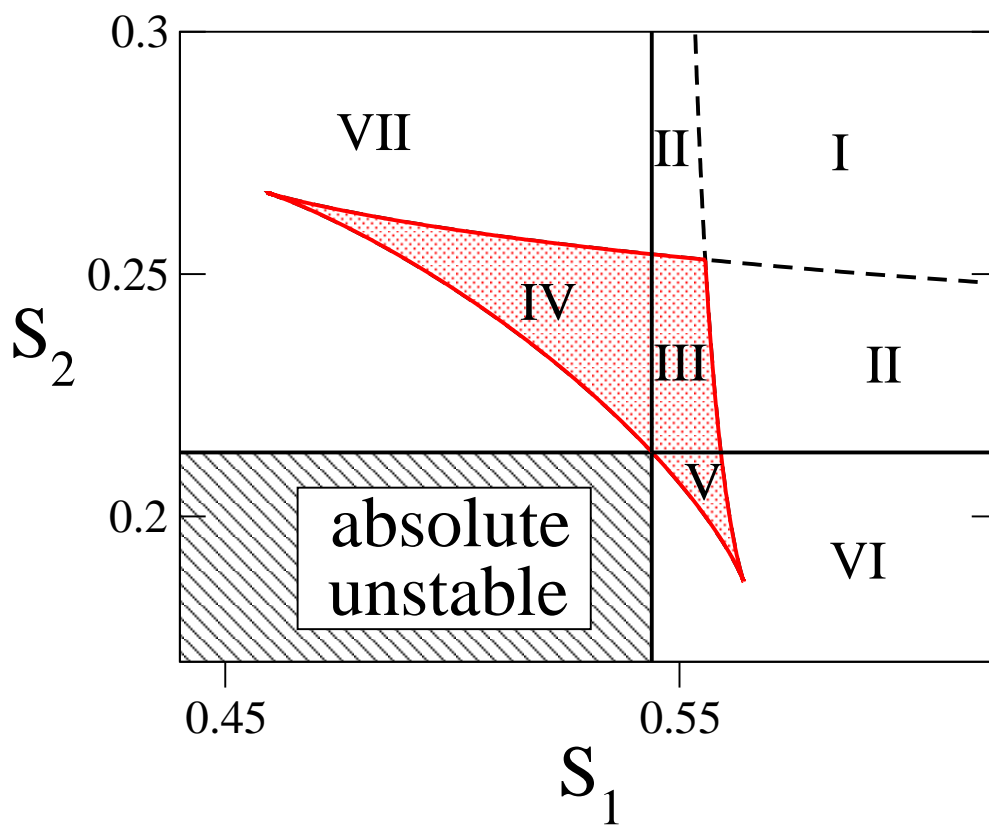


Fig. 5
 Pototsky et al., J. Chem. Phys.

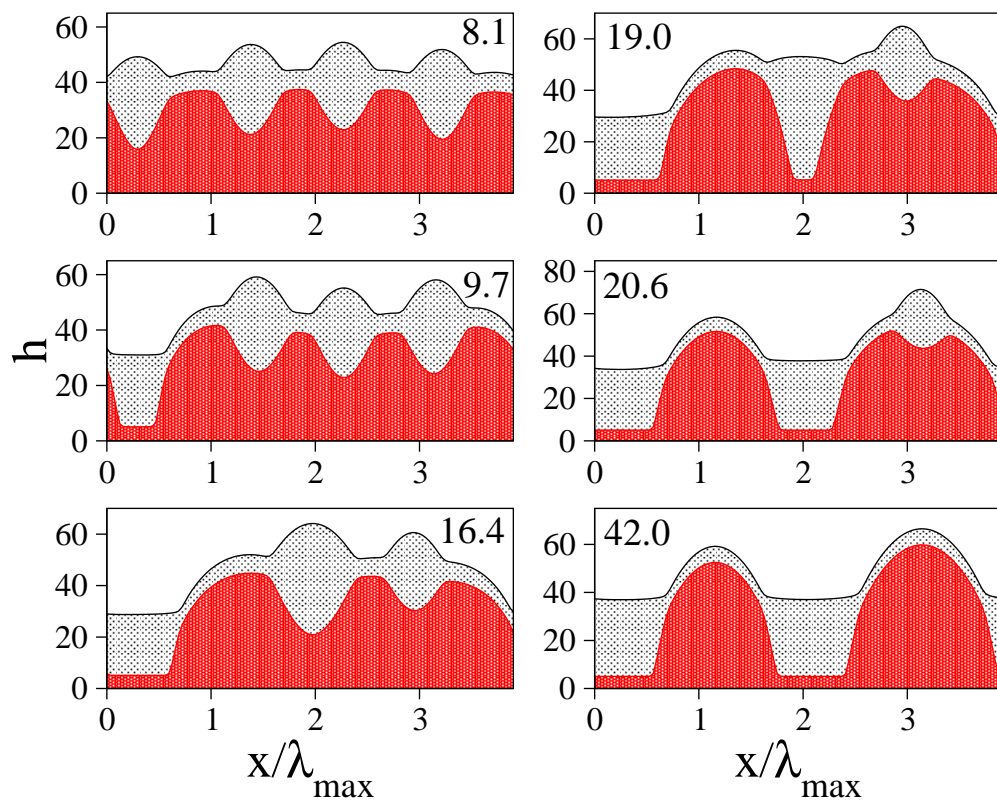


Fig. 6
 Pototsky et al., J. Chem. Phys.

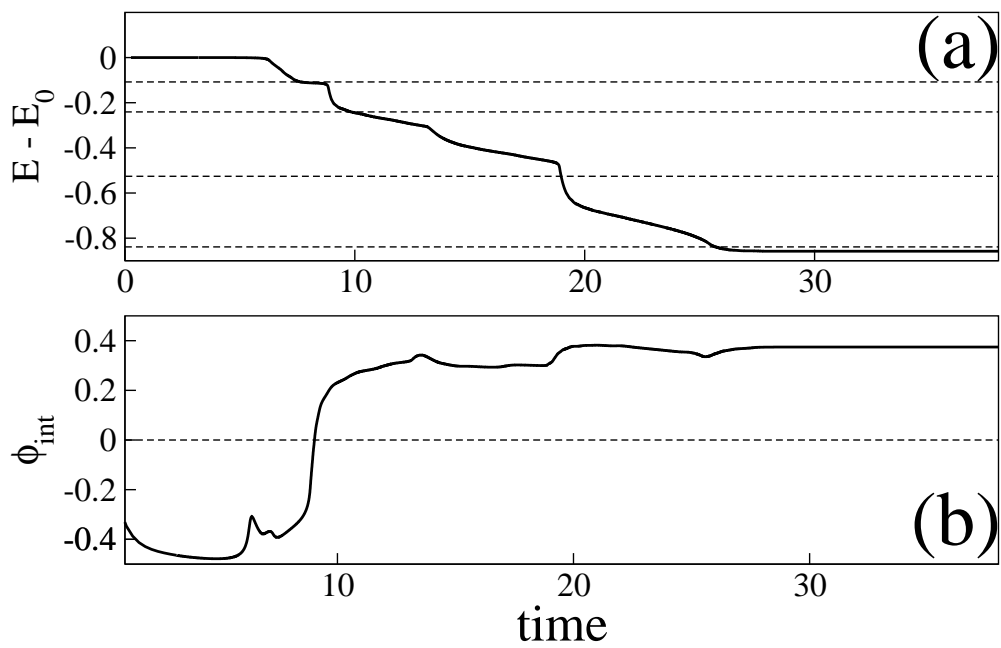


Fig. 7
Pototsky et al., J. Chem. Phys.

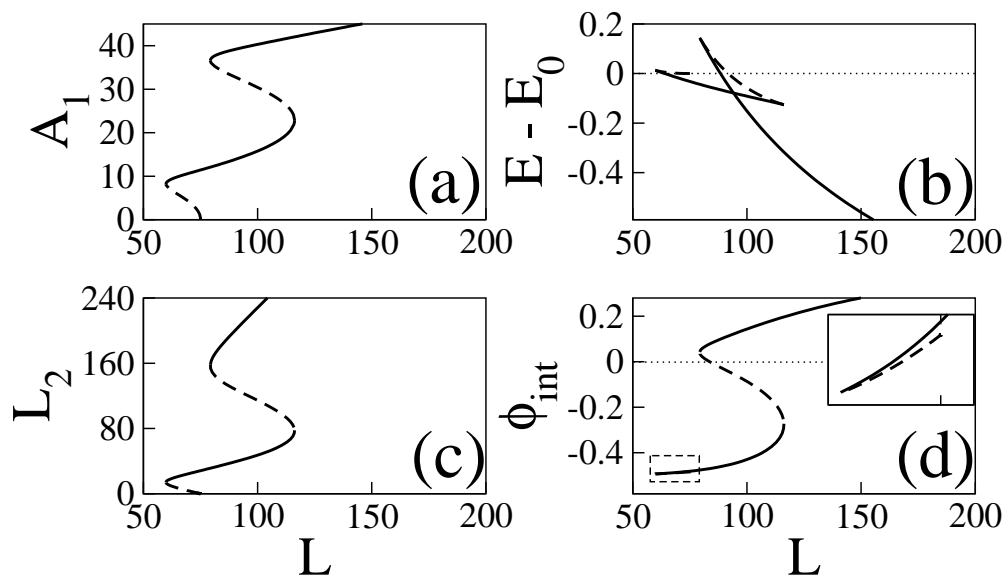


Fig. 8
 Pototsky et al., J. Chem. Phys.

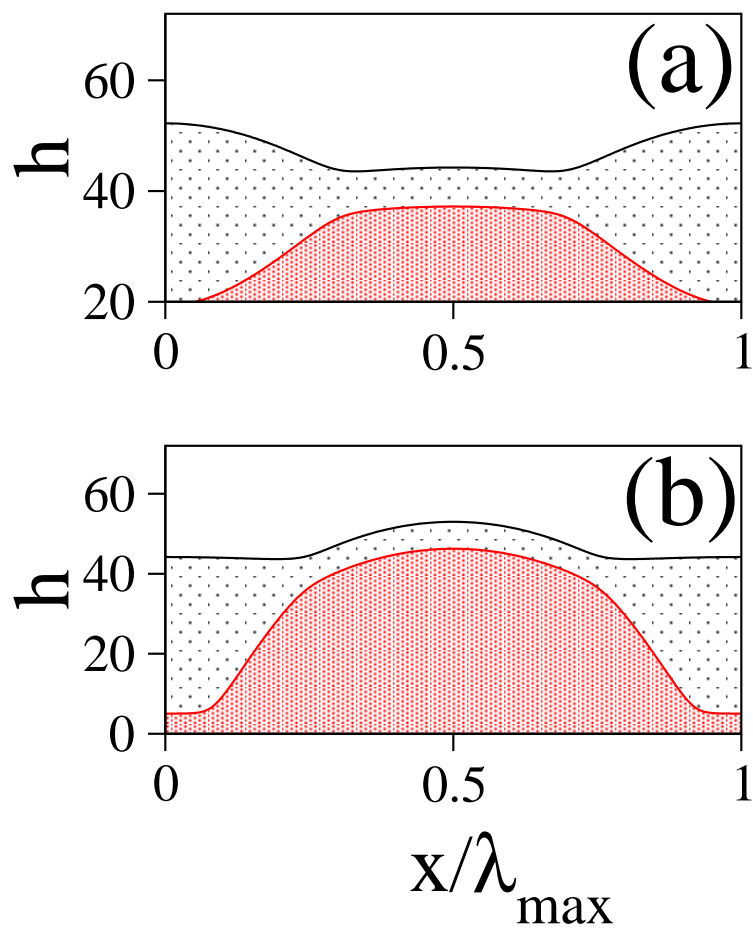


Fig. 9
Pototsky et al., J. Chem. Phys.

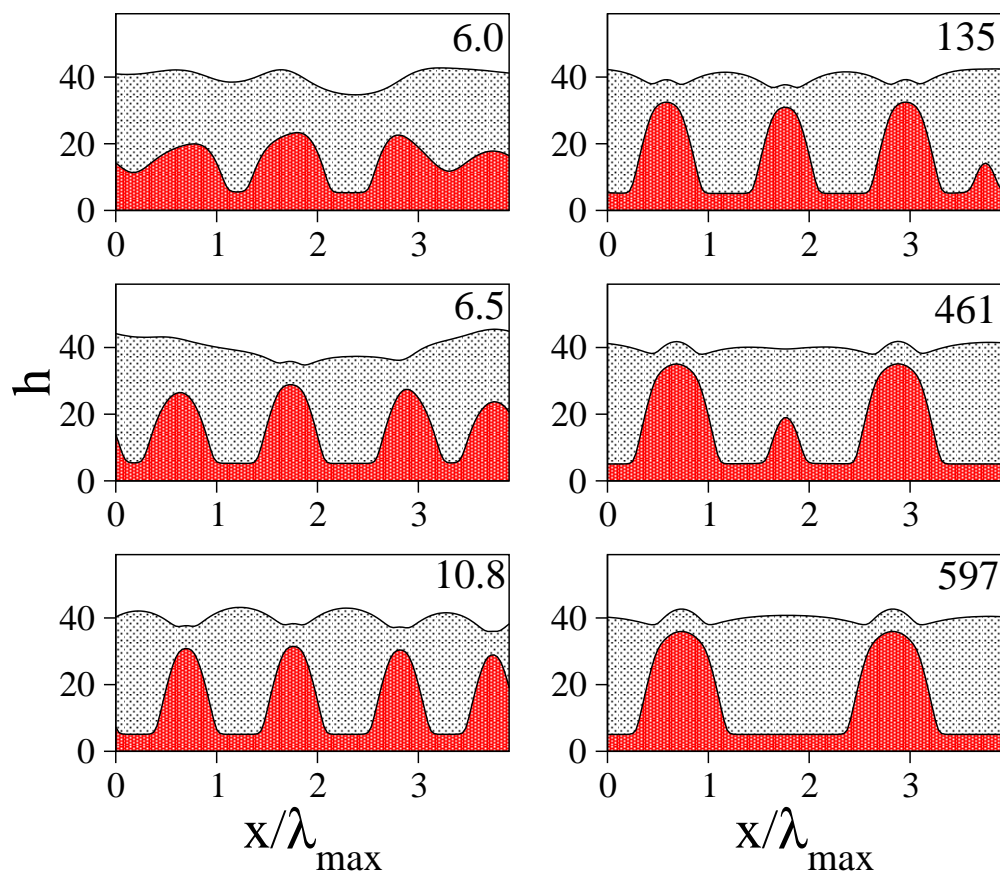


Fig. 10
 Pototsky et al., J. Chem. Phys.

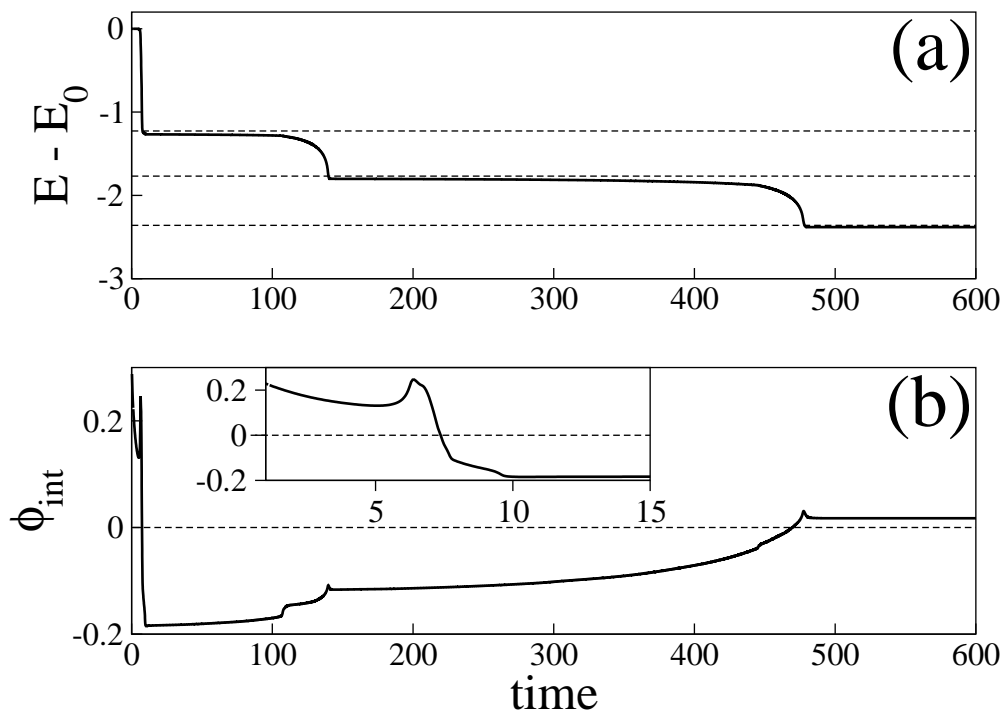


Fig. 11
Pototsky et al., J. Chem. Phys.

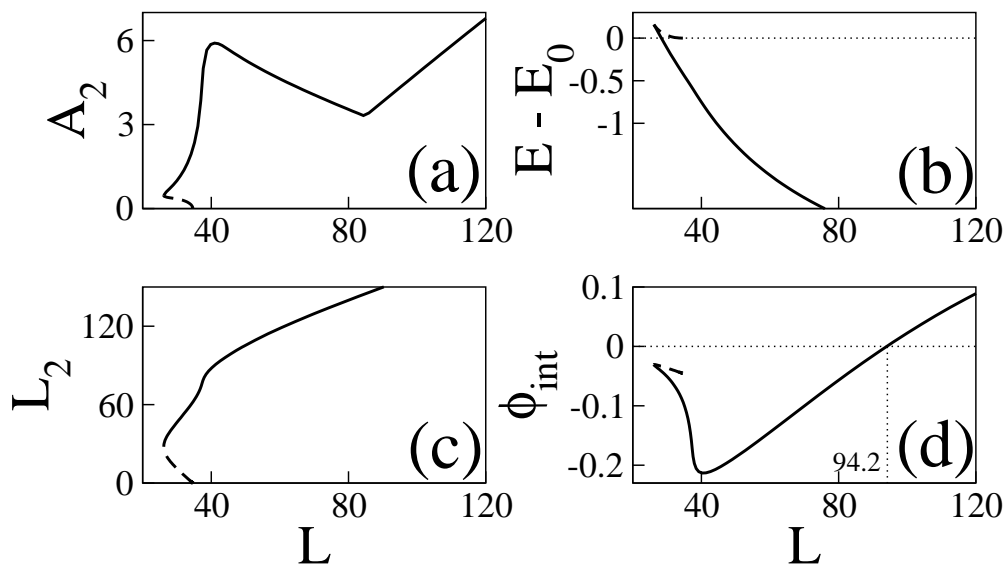


Fig. 12
 Pototsky et al., J. Chem. Phys.

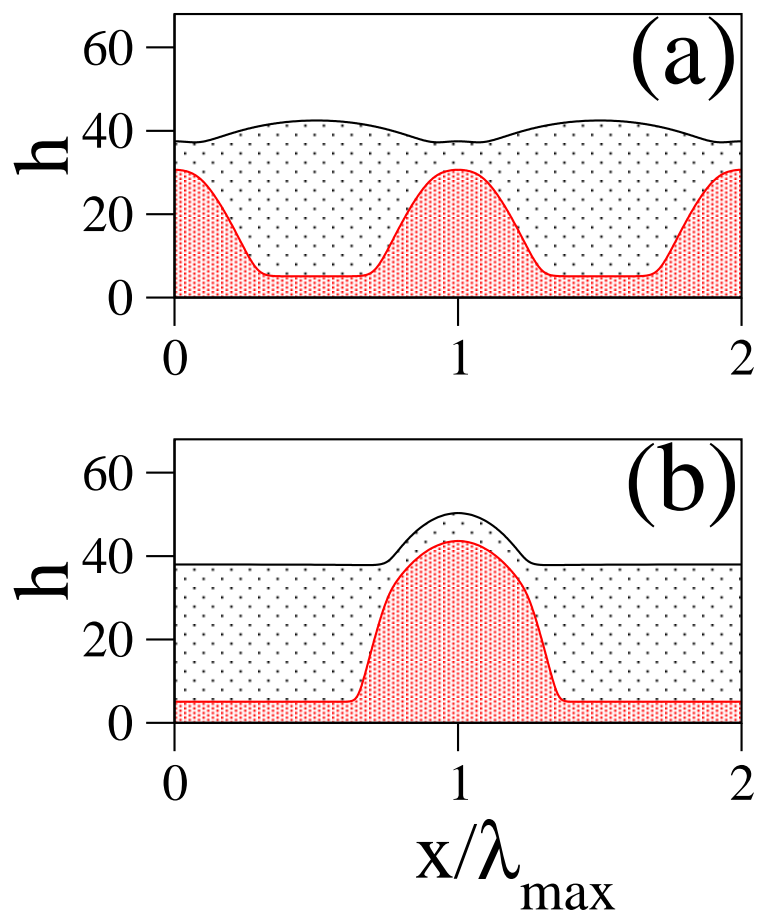


Fig. 13
Pototsky et al., J. Chem. Phys.

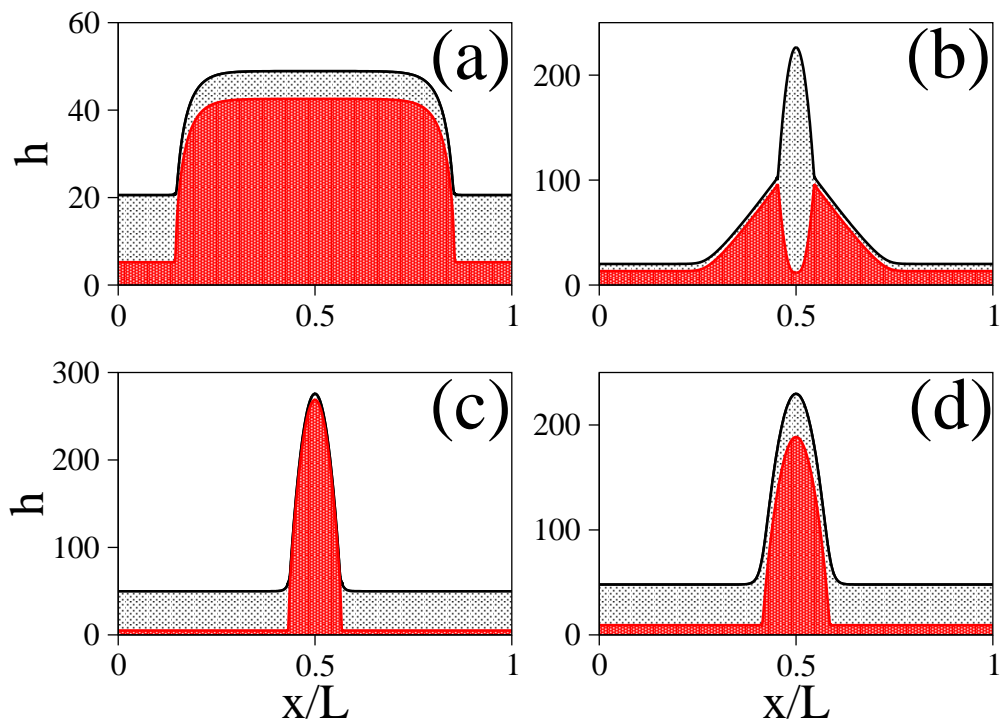


Fig. 14
 Pototsky et al., J. Chem. Phys.

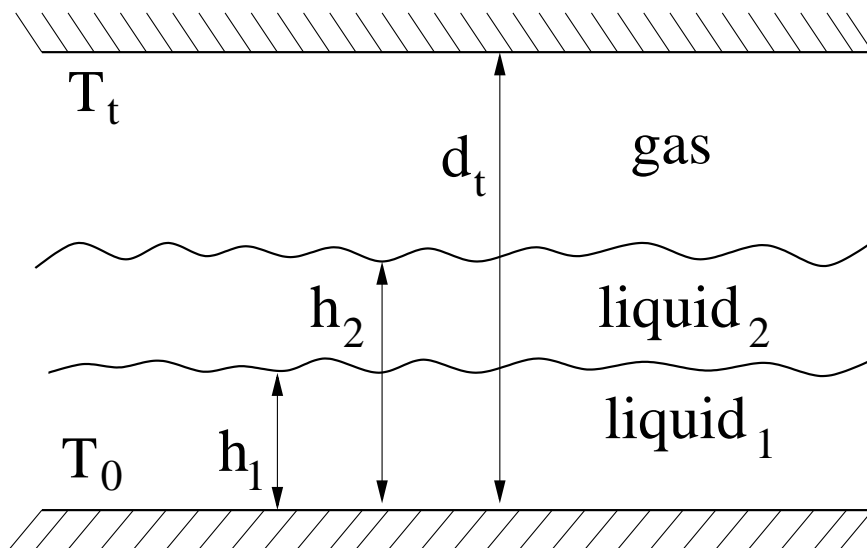


Fig. 15
Pototsky et al., J. Chem. Phys.